Liang Jun (Orcid ID: 0000-0002-4590-2978)
Reimer Ashton, S (Orcid ID: 0000-0002-4621-3453)
Hampton Donald L. (Orcid ID: 0000-0002-4893-5791)
Zou Shasha (Orcid ID: 0000-0001-7726-2349)
Varney Roger (Orcid ID: 0000-0002-5976-2638)

Ionospheric electron heating associated with pulsating auroras: Joint optical and PFISR observations

Jun Liang[1], E. Donovan[1], A. Reimer[2], D. Hampton[3], S. Zou[4], and R. Varney[2]

1. Department of Physics & Astronomy, University of Calgary, Canada

2. Stanford Research Institute, CA.

3. Geophysical Institute, University of Alaska Fairbanks, AK

4. Department of Climate and Space Sciences and Engineering, University of Michigan, MI

Submitted to J. Geophys. Res — Space Physics

Email: liangj@ucalgary.ca

Revised on 26 April 2018.

Abstract. In a recent study, Liang et al. [2017] repeatedly identified strong electron temperature (T_e) enhancements when Swarm satellites traversed pulsating auroral patches. In this study, we use joint optical and Poker Flat Incoherent Scatter Radar (PFISR) observations to further investigate the F-region plasma signatures related to pulsating auroras. On 19 March 2015 night which contained multiple intervals of pulsating auroral activities, we identify a statistical trend, albeit not a one-to-one correspondence, of strong T_e enhancements (~500-1000 K) in the upper F-region ionosphere during the passages of pulsating auroras over PFISR. On the other hand, there is no discernible and repeatable density enhancement in the upper F-region during pulsating auroral intervals. Collocated optical and NOAA satellite observations suggest that the pulsating auroras are composed of energetic electron precipitation with characteristic energy >10 keV, which is inefficient in electron heating in the upper F-region. Based upon PFISR observations and simulations from Liang et al. [2017] model, we propose that thermal conduction from the topside ionosphere, which is heated by precipitating low-energy electrons, offers the most likely explanation for the observed electron heating in the upper F-region associated with pulsating auroras. Such a heating mechanism is similar to that underlying the "stable auroral red arcs" in the subauroral ionosphere. Our proposal conforms to the notion on the co-existence of an enhanced cold plasma population and the energetic electron precipitation, in magnetospheric flux tubes threading the pulsating auroral patch. In addition, we find a trend of enhanced ion upflows during pulsating auroral intervals.

1. Introduction

The energy carried by electron precipitation dissipates in the Earth's ionosphere in three major ways, ionization, auroral excitation, and heating. For auroral phenomena, the main component of the primary precipitation typically consists of electrons on the order of keV up to a few tens of keV. For those primary electrons, energy loss is dominated by ionization and optically allowed excitation of neutral constituents, while direct heat transfer from the precipitation electrons to the ambient ionospheric electron gas is negligible. The primary electrons lose energy through collisions with ambient neutrals, which produces the resultant secondary electrons. The secondary electrons may further lose energies through collisions with neutrals during their transport in the ionosphere. When the energy of secondary electrons is degraded to several eV, energy loss to ambient ionospheric electrons becomes important and therefore acts to elevate the ionospheric electron temperature (T_e) [e.g., *Rees and Jones*, 1973; *Schunk and Nagy*, 1978]. This secondary electron heating is a local effect, meaning that the heating occurs only where the secondary electrons are present. Impact ionization and 630 nm red-line auroral emissions are expected to coexist with the heating. The secondary heating mechanism is sensitive to the characteristic energy of the primary precipitation: the higher the energy of precipitating electrons, the lower the secondary electron production rate at higher altitudes, and in turn the less heating effect there.

On the other hand, if the downgoing magnetospheric electrons include a component of substantially "colder" electrons, e.g., on order of ~10 eV or less, electron heating in the upper

ionosphere may operate in a fundamentally different way. The "cold" magnetospheric electrons cannot penetrate deeply into the ionosphere, but can strongly heat electrons near the topside boundary of the ionosphere. The heat will be conducted toward lower altitudes into the F-region ionosphere. In this scenario, the T_e enhancement seen in the F-region ionosphere is a remote effect, meaning that the low-energy magnetospheric electrons do not actually penetrate to F-region altitudes, so no significant ionization or red-line auroral excitation is expected to accompany the heating there. However, the change of T_e profile would affect the plasma density in the upper F-region, e.g., due to T_e-dependent recombination rates of ions [e.g., *Bekerat et al*, 2007; *David et al*., 2011; *Zhu et al*., 2016; *Zou et al*., 2017]. Also, when T_e is sufficiently high the high-energy tail in the thermal distribution of electrons may exceed the excitation threshold of $O(^1D)$ and cause some moderate 630 nm emissions [*Solomon et al*., 1988]. However, the changes in plasma density and red-line intensities described above are presumably smaller than those in the secondary electron heating scenario, for the same level of T_e enhancement. A heat conduction scenario proceeded by magnetospheric cold electrons has been recognized as the driving mechanism of the strong F-region T_e enhancement in the stable auroral red (SAR) arc phenomenon in the storm-time subauroral ionosphere [*Roble and Reses*, 1975; *Kozyra et al.*, 1990; *Fok et al.*, 1991].

It is possible for the above two heating mechanisms to coexist. If one is to elect an auroral phenomenon that may involve a mixture of energetic electron precipitation and low-energy electron content from the magnetosphere, the pulsating aurora is arguably the most probable

candidate. A pulsating aurora is a repetitive modulation of auroral luminosity with periods typically of the order of ~3-30 sec [*Royrvik and Davis*, 1977; *Johnstone*, 1978]. It can be divided into two categories, one characterized by well-defined and repeatedly identifiable patch structures that follow E×B convection, and the other is a more dynamic type with rapidly changing shapes and locations, yet lacking repeatable patch structures [*Grono et al*., 2017]. The former category is more often observed and will be of exclusive interest in this study. Pulsating auroras are typically excited by electron precipitation with energies ranging from several keV up to hundreds of keV [*Sandahl et al*., 1980; *Yau et al*., 1981; *Jones et al*., 2009; *Nishimura et al*., 2011; *Lessard*, 2012; *Jaynes et al*., 2013; *Samara et al*., 2015]. In addition to such an energetic electron component, a pulsating aurora patch has long been hypothesized to connect to magnetospheric flux tubes filled with enhanced "cold" plasma contents [*Johnstone*, 1978; *Davidson*, 1990; *Demekhov and Trakhtengerts*, 1994; *Liang et al*., 2015] --- the underlying rationale of such a hypothesis will be discussed later in Section 5. Pulsating auroras do not exhibit a particularly strong optical luminosity, hinting at a limited energy flux of the precipitation [*Royrvik and Davis*, 1977]. The FAC intensity within pulsating auroral patches was also found to be moderate only, with peak magnitude of at most a couple of $\mu A/m^2$ [*Gillies et al*., 2015; *Liang et al*., 2017, hereafter referred to as LJ17].

The energetic electron precipitation characteristic of the pulsating auroras produces substantial ionization and heating effect in the E-region [*Jones et al*., 2009; *Hosokawa and Ogawa*, 2015; this study] or the D-region ionosphere [*Miyoshi et al*., 2015; *Oyama et al*., 2107],

but their role in electron heating in the upper F-region is not expected to be significant. However, LJ17, a study closely related to the current paper, conducted a survey of Swarm satellite (~460 km altitude) data and, in a majority of the events, a strong electron temperature (T_e) enhancement was identified when the Swarm footprint traversed pulsating auroral patches. The observation of T_e enhancement was not contingent upon whether the pulsating patch was "on" or "off" at the satellite traversal epoch. LJ17 also performed a numerical simulation to explore the potential mechanisms underlying the electron heating associated with the pulsating aurora. Using these simulations, it was found that, in a majority of the Swarm events, the T_e enhancements can be explained if there exists a heat flux input of the order of ~10^{10} eV/cm^2/s at the topside boundary of the ionosphere. It was suggested that such heat fluxes would be led by "cold" magnetospheric electrons (on order of ~10 eV or less) embedded in magnetic flux tubes threading the pulsating aurora. These cold magnetospheric electrons collide with and transfer heat to the topside boundary of the ionosphere, and the heat is then conducted downward into the F-region ionosphere. This proposal is consistent with existing theories of pulsating auroras, specifically the co-existence of an enhanced cold magnetospheric plasma population in addition to the energetic electron precipitation.

The LJ17 study recognized some uncertainties associated with satellite measurements. First, Swarm satellites provide only one-point measurements. Thus, the possibility that the T_e enhancement in the upper F-region being led by thermal conduction from the E-region ionosphere, which is heated by the pulsating auroral precipitation, could not be ruled out.

Furthermore, the possible role of secondary electron heating associated with pulsating auroras could not be fully examined in LJ17. Therefore, it is desirable to have concurrent and collocated red-line aurora observations to better distinguish between the secondary electron heating mechanism and the thermal conduction mechanism in the F-region ionosphere. The above concerns motivated the current study to utilize joint radar and multi-wavelength auroral observation instruments.

Incoherent scatter radar (ISR) measurements have been previously used in the studies of pulsating auroras. *Jones et al*. [2009] compared the electron density (N_e) profile from PFISR data with the electron precipitation spectrum measured by ROPA rocket mission during pulsating auroral intervals. *Hosokawa and Ogawa* [2015] and *Miyoshi et al*. [2015] studied the variation of ionospheric N_e associated with pulsating auroras using joint optical and EISCAT data. *Hosokawa et al*. [2010; 2012] found the modulation of ionospheric electric fields and conductances by pulsating auroras. However, the above studies were all limited to the E-region and/or D-region ionosphere where most of the energies carried by pulsating auroral electron precipitation are deposited. *Oyama et al*. [2014] investigated the high-latitude ionospheric variations in the vicinity of poleward-expanding auroras during substorms using EISCAT data. They noticed that, during the early recovery phase N_e features a large peak in the E region and a statistically smaller peak in the F region. They attributed the E-region N_e peak to hard electron precipitation, possibly associated with pulsating auroras, and suggested that the weak F-region peak at 250-300 km altitude might be caused by soft electron precipitation of order of ~100 eV. However, *Oyama et*

al. [2014] did not utilize optical observations, nor did the statistical result address whether the hard and soft electron precipitations typically coexist or are independent of each other. To the best of the authors' knowledge, a dedicated study of F-region plasma signatures related to pulsating auroras using joint optical and ISR data is lacking in the literature.

The study presented in this paper is intended to expand upon the previous work of LJ17. The variations of ionospheric parameters, including T_e , N_e , and ion upflows etc., as observed by Poker Flat Incoherent Scatter Radar (PFISR) during a 2-hr interval, will be presented. The interval consisted of multiple pulsating auroral activities. With the aid of the concurrent and co-located optical auroral measurements from the Meridian Spectrograph at Poker Flat (PFMSP), we distinguish and compare the ionospheric variations during pulsating auroral intervals and red-line auroral intensification intervals. We find that the observed T_e enhancement in the upper F-region (~300-600 km) associated with pulsating auroras is unlikely to be produced by either thermal conduction from the heated E-region ionosphere, or the secondary electron heating led by the primary energetic electron precipitation. The data presented in this study support the proposal in LJ17 that, the T_e enhancement in the upper F-region ionosphere associated with pulsating auroras are likely produced by thermal conduction from the topside ionosphere, where the electrons are heated by collisions with magnetospheric low-energy electrons. This is consistent with the coexistence of a low-energy plasma population in addition to the energetic pulsating auroral precipitation, in magnetospheric flux tubes threading the pulsating auroral patch. We also observe a trend of enhanced ion upward flows during pulsating auroral intervals,

and suggest that the strong T_e enhancement associated with pulsating auroras may act as one potential mechanism driving ion outflows in the nightside auroral ionosphere.

2. Instruments

The main instruments to be used in this study include PFISR and PFMSP, both located at Poker Flat Research Range (65.13° N, 147.47° W Geo.), as well as THEMIS all-sky-imager (ASI) at Fort Yukon (66.56° N, 145.22° W Geo.). The event of interest occurred on 19 March, 2015, during the recovery phase of St. Patrick's Day geomagnetic storm. During the event, PFISR was run in two different experiment modes: before 13 UT a 5-beam mode called Freg732_v01 was run, and after 13 UT an 11-beam mode called WorldDay35 was run. Figure 1a shows the elevation angles and the azimuths of the beams in two experiment modes, and Figure 1b shows the projection of the beams onto the Altitude-Adjusted Corrected Geomagnetic (AACGM) coordinates. Throughout this study, the magnetic latitude and longitude (MLAT/MLON) are defined according to AACGM coordinates with IGRF12 coefficients, so that the beam (except for the field-aligned one) maps to different MLAT at different height. Among those beams, beam-1 from the Freg732_v01 experiment and beam-7 in the WorldDay35 experiment are along the same vertical direction, while beam-3 in the Freg732_v01 experiment and beam-11 in the WorldDay35 experiment are along the same field-aligned direction. We shall refer to these beams as the vertical (sometimes abbreviated as VERT) beam and field-aligned (sometimes abbreviated as FA) beam, respectively, for the remainder of this study. Data from

these two beams will be used to construct an altitude profile of ionospheric parameters such as T_e and N_e. In the Freg732_v01 experiment a dual long pulse (480 μs) is transmitted, while the WorldDay35 experiment transmits both an alternating-coded pulse (480 μs long pulse with 30 μs bauds) and a 330 μs long pulse. The long pulse and alternating coded pulse are suitable for the study of the F-region and E-region ionosphere, respectively. Since the core research target in this study is the T_e enhancement in the upper F-region, long-pulse data will be focused on. All PFISR data used in this study are specifically processed and carefully calibrated by the data provider. In the PFISR data processing, the autocorrelation functions (ACF) of the received signal are fitted to model ACFs derived from the plasma wave theory of incoherent scatterers [e.g., *Evans*, 1969] convolved with the ambiguity function of the transmitted pulse to obtain the best-fit parameters from the ACF. Fitted data with large fitting errors may result from a variety of reasons, e.g., the inapplicability of the theoretical model to the actual scatter physics, inappropriately determined or specified ion compositions, or low signal-to-noise ratios. In this study, fitted data with error larger than the fitted value are discarded. For T_e, which is of core interest in this study, we perform two additional quality checks: (1) all Te >6000K data points are discarded; (2) any T_e data bin that is more than two times, or smaller than half, the mean value from its adjacent height bins (above and below) is discarded.

The integration time is ~74 sec for the Freg732_v01 long pulse mode, and ~70 sec for the WorldDay35 long pulse mode. Such integration times are much longer than the periods of pulsating auroras, so the integrated data represents an average over the on and off intervals of

pulsating auroras. We argue that the long integration time does not significantly hinder our research effort. As noted in LJ17, T_e enhancement at Swarm altitude (~500 km) is observed regardless of whether the pulsating patch is "on" or "off" at the epoch of satellite traversal. From a theoretical perspective, the electron cooling timescale in the upper F-region tends to be much longer than the pulsating period (~10 s in our event), such that a dramatic fluctuation of T_e over one or few on-off cycles of the pulsating aurora is not expected. More likely, T_e in the upper F-region would embody an averaged effect over many on/off cycles of the pulsating aurora. Furthermore, for each pulsating auroral activity interval we identified, there are actually multiple individual pulsating patches, and it generally takes ~10 min or more for the ensemble of pulsating auroral patches to pass over the PFISR beam. We thus expect that the T_e enhancement in the upper F-region associated with the pulsating auroral activity, the core research interest in this study, would overall be preserved in a PFISR measurement despite the comparatively long integration time. This is expected to be particularly true in a statistical sense as we shall discuss in Section 3.5. We however note that the Freg732_v01 experiment has the potential to produce data at higher time solution. Reprocessing of PFISR data with an integration time of 10 sec or less, which would be useful in unveiling the fine-scale variations of ionosphere parameters associated with pulsating auroras [*Hosokawa and Ogawa*, 2015], is now under investigation by the data provider.

The Poker Flat Meridian Spectrograph is based on the CEDAR Optical Tomographic Imaging Facility (COTIF) design (Semeter, et al., 1999). The imaging spectrograph acquires an

image of the full spectral range from 390 to 750 nm along the local magnetic meridian every 13.6 seconds. The background subtracted intensities of four basic auroral emissions – the atomic oxygen red-line (630 nm) and green-line (557.7 nm), the N2+ First Negative blue-line (427.8 nm), and the Balmer beta emission of H (486.1 nm) – are extracted at 180 elevation bins. Since the intensity profiles are collected along the magnetic meridian they facilitate a direct comparison with the PFISR observations on its magnetic-northward pointing beams.

The all-sky imager (ASI) [*Donovan et al.*, 2006] of the Time History of Events and Macroscale Interactions during Substorms (THEMIS) mission will be used in this study to identify pulsating auroral activities and their passage over PFISR beams. THEMIS ASI captures whitelight auroral images at a 3-second cadence with exposure time of 1 sec. An emission altitude of 105 km is assumed for the ASI mapping throughout this study.

We shall also use the NOAA's Polar Orbiting Environmental Satellite (POES) data to evaluate the characteristic energy of pulsating auroral electron precipitation. Two major instruments of NOAA/POES used in this study are the total energy detector (TED) and the Medium Energy Proton and Electron Detector (MEPED). The TED instrument measures the precipitation fluxes of electrons and protons over an energy range from 50 eV to 20 keV. TED contains two sensors: a 0^0-sensor mounted to view roughly along the radial vector of the probe, and a 30^0-sensor mounted to view in a direction 30° off the zenith. At auroral latitudes, the two sensor directions are both inside the downward loss cone and can thus be combined to calculate the total precipitating flux. Though TED does not measure the detailed energy spectrum of

precipitating particles, it provides the information of the energy bin containing the maximum differential flux, which offers a clue on the "characteristic energy" of the precipitation. The MEPED instrument monitors directional fluxes of protons and electrons with energies from >30 keV up to several MeV. Two identical solid-state telescopes are onboard NOAA/POES satellite. The 0^0 telescope is mounted to view roughly along the radial direction, while the 90^0 telescope is mounted to view in a direction roughly perpendicular to the 0° detector. In principle, the particles monitored by the MEPED 0^0- and 90^0- telescopes will owe their origins to the particles inside and just outside the loss-cone, respectively, in the equatorial magnetosphere.

3. Observations

In this section we shall present the joint optical and radar observations of various auroral activities around Poker Flat during ~12-14 UT on 19 March 2015, with a focus on the F-region electron heating effect associated with pulsating auroras. First, the data collection methods and analysis for a few radar beams during selected auroral activity intervals are presented. Next, a statistical analysis is presented. While not presented as part of the analysis, plots of T_e and N_e for all available PFISR beams during the entire event interval of interest (including both experiment modes) are available as supplementary material. The complementary datasets from the NOAA/ POES satellite, AMPERE, and the AMIE model are also presented and strengthen some of our main arguments and conclusions.

3.1 Panorama of optical auroras

The top of the Figure 2 shows the keogram of the THEMIS whitelight ASI at Fort Yukon. Readers are referred to the supplementary movie to view the full record of auroras. Initially, the auroras were mainly characterized by some bright structures such as arcs and streamers. There were some hints of pulsating auroras before 1218 UT, but they were either well south of PFISR, or coexisting yet overridden in intensity by other much brighter, non-pulsating auroral structures. Clear signatures of pulsating auroras over PFISR are observed after ~1218 UT, which manifested as intermittent "streaks" in the keogram. While there were some gaps, the pulsating auroral activities around PFISR on overall lasted for ~1.2 hours, and faded after ~1330 UT. Three pronounced intervals of pulsating auroras that were active over the PFISR field-of-view are marked in the top panel.

The second to bottom panels of Figure 2 show the observations of the red-line (630 nm), the green-line (557.7 nm), and the blue-line (427.8 nm) auroras from PFMSP. Even with the ~14 s temporal resolution of PFMSP, the pulsating variation of auroras are visible in green-and blue-line auroras, whereas there is a lack of discernible pulsating auroras in the red-line emission data in this event. There are however, a few bright red-line auroral structures in this event, which will also be part of our research interest in this study (e.g., section 3.4).

3.2 T_e enhancement associated with pulsating auroras and red-line auroral intensifications: Examples on the field-aligned beam.

In this subsection we will introduce our main research interest and demonstrate the way how to identify intervals of pulsating auroras and red-line auroral intensifications. We shall exemplify

with the field-aligned beam (beam-3 in Freg732_v01 experimental mode). For this beam, all altitude bins map to essentially the same MLAT/MLON, such that beam measurements in the upper F-region are conjugate to the auroras passing over the beam. To present the temporal variation of optical auroras over the beam, we sample and average the auroral intensity from THEMIS ASI within $\pm 0.05^0$ MLAT and $\pm 0.2^0$ MLON around the beam, and present it in the top panel of Figure 3. The existence of pulsating auroral activities can be readily discerned in this plot via the presence of higher-frequency (periods <30s), small-scale oscillations superimposed on ambient variations. In the second panel, we display the auroral intensities at three emission lines, 427.8 nm, 557.7 nm, and 630.0 nm, from the PFMSP data sampled in the elevation bin along the same field-aligned direction as the beam. The third panel of Figure 3 shows the T_e measurement, the key parameter of interest in this study. We have also plotted the N_e measurement in the bottom panel of the figure, but dedicated discussions on the N_e variations associated with auroras is to be presented in Section 3.4.

As one can see, T_e in the upper F-region (~300-600 km altitude), the main research object in this study, is in general enhanced during actively auroral intervals, as compared to the T_e during relatively quiet intervals. However, we shall clarify that, it is incorrect to assume that T_e enhancement is proportional to the auroral brightness (or equivalently the electron precipitation flux), with no dependence on the type of aurora. As an example, consider the strong auroral peak at ~1150 UT, which is led by the passage of a non-pulsating, bright auroral spiral over the beam (see the supplementary movie). There is a moderate red-line auroral intensification, but the red-

to-blue intensity ratio is very low, implying a high characteristic energy of precipitation. The peak auroral intensity in green/blue emissions of this structure is higher than that of the subsequent pulsating auroras, yet the associated T_e enhancement is weak only.

Upon a browse over PFISR and auroral observations on all beams during the event interval, we note that, while occasional exception exists strong T_e enhancements are mainly seen during the following two classes of auroral activities. A more detailed statistical examination in this regard will be given later in Section 3.5 later.

(a) The red-line auroral intensification (marked by arrows in Figure 3), in practice discerned by a distinct peak of PFMSP 630 nm auroras over background values. This could be caused either by a strong intensification of the total electron precipitation flux as reflected in strong peaks in blue/green line emissions (e.g., the ~1204 UT peak), or by a relatively low characteristic energy of precipitation as hinted by an elevated red-to-blue intensity ratio (e.g., the ~1215 UT peak). In both scenarios, there is supposed to be a strong enhancement of secondary electron fluxes in the F-region ionosphere, contributing to the red-line auroral intensification and electron heating there.

(b) The pulsating aurora, whose existence can be inferred from the time series of sampled THEMSI ASI counts (see top panel of Figure 3) via the presence of smaller-scale oscillations superimposed on ambient variations. The intervals of pulsating auroral activities are indicated with vertical dotted lines in the figure. T_e in the upper F-region on overall enhances during the

pulsating auroral interval. Note that each pulsating auroral interval is typically comprised of intermittent passage of numerous individual patches. Also, as noted in LJ17, substantial T_e enhancement exists in 70% of their pulsating auroral patch events. Therefore, occasional brief gaps of T_e enhancement during the marked pulsating auroral interval are understandable. As we shall elaborate in Section 3.5, the percentage of PFISR data points that feature noticeable T_e enhancements in the upper F-region is also found to be ~70% during pulsating auroral intervals.

Two important notes need to be clarified here. First, while red-line auroral intensification intervals are selected according to PFMSP 630 nm observations, we notice that such intervals may at times coexist with pulsating auroral activities. For example, in the supplementary auroral movie one may notice that the auroral intensifications around ~1205 UT appear to be a mixture of a much stronger streamer-like auroral brightening and some weaker pulsating auroras in the background. Under such a mixture, it is difficult to unequivocally discriminate the respective role of each type of aurora on the ionospheric electron heating, although we speculate that the red-line auroral intensification should dominate the contribution. In this study, when there is a coexistence of strong red-line intensification and weaker pulsating auroras, we classify it as the former only. We limit our specification of pulsating auroral intervals to those accompanied by moderate red-line auroral intensity only (persistently <2 kR and without any notable peak). By way of such classification we have limited the pulsating auroral precipitation under investigation to be dominantly composed of energetic electron precipitation (see also Section 4.1).

Secondly, while in a few cases the red-line intensification is quickly followed by pulsating auroras, it is wrong to assume that the observed T_e enhancement during the latter interval is a remnant of the former activity, due to the cooling time lag of ionospheric electrons. One should interpret that the variations seen on a single beam as mostly representing the passage of drifting ionospheric structures through the beam. The life time of the T_e remnants of the previous activity is contingent upon the electron cooling timescale or the drift timescale over an individual beam, whichever is shorter. Neither of the two timescales is expected to exceed a few minutes based upon our evaluation form available data and LJ17 simulation. Thus, the enduring T_e enhancements during the pulsating auroral interval (>10 min) are unlikely to represent the remnant effects of the preceding auroral intensification; the pulsating auroral activity should by itself provide a heating source for the upper F-region electrons.

3.3 Spatial-temporal variation of pulsating auroras and T_e enhancement

PFISR switched to the WorldDay35 experiment mode after 13 UT, which contains 11 beams with denser spatial sampling, facilitating an investigation of the spatial-temporal variation of the T_e enhancement associated with pulsating auroras. After 13 UT, pulsating auroras are characterized by an overall eastward drift. This can be viewed directly from the supplementary movie, or in a more succinct way via the ewogram. An ewogram is a keogram taken in the east-west slices instead of north-south slices, enabling the visualization of east-west propagation of auroras (see, e.g., *Yang et al*. [2015]). In Figure 4, we plot the joint auroral and PFISR T_e observations on four beams: the vertical beam 7, the oblique meridional beam-9, and two lateral

beams 1 and 4 (see Figure 1 for beam geometry). The arrangement of sub-figures is similar to the realistic geometry of those beams in MLAT/MLON: the left/right/upper/bottom of the plot indicates the west/east/north/south directions, respectively. In each sub-figure, the top panel shows the auroral ewogram corresponding to the beam. We point out a caveat that, different altitudes along a beam map to different MLATs defined by AACGM coordinates. Since our prime research interest is the T_e variation in the upper F-region, for each beam, the auroral ewogram is sampled in the MLAT range corresponding to 300-500 km altitude bins of the beam, so that the sampled auroras are magnetically conjugate to the PFISR T_e in the upper F-region. The eastward motion of pulsating auroras can be inferred from the slope of the trace in the ewogram. The bottom panel of each subfigure displays the T_e observation on the respective beam. It is straightforward to notice a general correspondence between the pulsating auroral passage and the T_e enhancement in ~300-500 km altitude on each beam. Furthermore, the T_e enhancement appears earliest on the westernmost beam-1 (before ~1310 UT), subsequently on meridian beams (~1310-1325 UT), and the latest on the easternmost beam-4 (~1320-1330 UT). This indicates an eastward propagation of T_e enhancements, consistent with the motion of pulsating auroras. Other than the above long-lasting bulk pulsating auroral activity intervals, brief isolated passages of a single patch structure may also leave imprint on T_e . For example, the upper F-region T_e enhancement at ~1330 UT on beam 9 and ~1336 UT on beam 4, upon a careful look into the auroral images, may be attributed to a weak pulsating patch passing over the two beams.

Upon a close look one may also notice a difference between the T_e signatures on meridional beams: the T_e enhancement on the oblique beam-9 appears to be more altitudinally band-limited, namely that the T_e enhancement is confined within a relatively small altitudinal range, and that the altitude of enhancement tends to gradually decline with time. The above feature can be explained as a combined effect of the tilt of the auroral patch structure, the eastward propagation of the patch, and the obliqueness of the beam. As one may see in the supplementary movie, most of the auroral patches during the interval of interest are tilted along the northeast-southwest direction. For an oblique beam, the limited altitude band of the T_e enhancement alludes to the limited MLAT width of the intersection between the patches and the beam. One can see an example shown in the middle of Figure 4. A tilted patch intersects the PFISR meridian at ~67.5^0 MLAT (corresponding to ~340 km altitude on beam-9) at 1316 UT, meanwhile a T_e enhancement is indeed found to peak at ~340 km altitude on beam-9. While the patch itself actually propagates eastward, due to its tilt the intersection between the patch and the PFISR meridian line would have an apparent southward (downward) motion in MLAT (altitude) along an oblique beam. When the beam-patch intersection drops to <300 km altitudes, the T_e enhancement in the upper F-region may no longer be seen. In comparison, the T_e enhancement on the vertical beam-7 tends to be broader in altitudes, since the MLAT difference across altitudes is small for the vertical beam.

To summarize the above observations, via multi-beam analysis we find that the spatial-temporal variations of PFISR T_e enhancements show general correspondence with the passages

of pulsating auroras over PFISR beams. This result offers another piece of evidence on the linkage between the pulsating aurora and the T_e enhancement in the upper F-region ionosphere.

3.4 N_e variation associated with red-line auroral intensification and pulsating aurora

We shall now check one other key parameter of the ionosphere, the electron density *N*e. In this subsection we shall demonstrate the N_e enhancement associated with the red-line auroral intensification, and compare to that during pulsating auroral intervals. PFISR N_e observation on the field-aligned beam during 1140-1300 UT was already given in Figure 3. In that figure, we have marked the one-to-one correspondence between the red-line auroral intensification, T_e enhancement, and N_e enhancement in the F-region ionosphere. For some short-lived red-line auroral intensification, the peak N_e enhancement in the upper F-region may appear to slightly lag the red-line intensification (e.g., for the ~1215 UT intensification). The correspondence between the red-line auroral intensification and the N_e enhancement in the upper F-region are readily understandable, since they are presumably attributed to the same mechanism, i.e., soft electron precipitation and/or secondary electrons of primary precipitation. The rise time of N_e in response to impact ionization is controlled by the recombination rate, which is relatively slow in the upper F-region at above 300 km altitudes. On the other hand, the 630 nm auroral intensity recorded by PFMSP represents an integral along the line-of-sight direction, and the peak contribution usually comes from lower altitude (<250 km) where the $O\ (^1D)$ quench rate is faster, leading to a shorter response time of the red-line aurora to the precipitation. This would explain the time lag between

the red-line auroral intensification seen on PFMSP and the peak N_e enhancement at >300 km altitudes in some cases.

Figure 5 demonstrates another pronounced red-line auroral structure during ~1320-1330 UT, which originates well poleward of Poker Flat and features a southward motion. We speculate that the intensification might be traced back to the streamer-like activity stemmed from in the poleward portion of the ASI field-of-view at ~1317 UT (see supplementary movie), which subsequently evolves eastward and southward and touches the northward-most beam-10 at ~1319 UT. In the top panel of Figure 5a, we plot the red-line auroral observation on PFMSP and mark the structure of interest. The 2nd panel shows the THEMIS white-light ASI counts sampled around the vertical beam. When the red-line structure reaches the PFMSP nadir at ~1326 UT, a corresponding intensity peak is also seen on THEMIS ASI. Such an auroral intensification is however non-pulsating, as evidenced by the absence of superimposed high-frequency oscillations, in contrast to the preceding pulsating auroral interval.

Figure 5b displays the N_e observations from the five meridian beams (Beam 7-11) along the magnetic meridian. The panel is organized by the elevation angle of beams: the top panel shows the observation from beam-10 which has the lowest elevation angle and thus extends to the highest MLAT, while the bottom panel corresponds to the field-aligned beam-11. A density structure extending from E-region to F-region first appears on beam-10 at ~1318 UT, and reaches the field-aligned beam at ~1327 UT. Their trend of southward propagation is consistent with that of the red-line auroral structure. Upon a careful check, we have confirmed that the

appearance of such density structure on each beam roughly coincides with the passage time of the red-line auroral structure over the beam. It is thus certain that those density structures are directly related to the red-line auroral intensification. A density enhancement in the upper F-region, which is also likely associated with the red-line intensification, can be seen on the vertical beam, though the N_e peak at ~400 km altitude slightly lags the arrival of red-line intensification and the E-region N_e enhancement. This again can be interpreted by the different recombination timescales at different altitudes. One may also notice that, after 1330 UT when the overall auroral brightness fades, there are still some noticeable N_e enhancement structures. A detailed exploration on the cause of those N_e structures after 1330 UT is beyond the research interest of this paper, but it leads us to exclude them when we collect "quiet interval" N_e for statistics in the next subsection.

We have also marked in Figure 5b the passage intervals of pulsating auroras over 300-500 km altitudes of beam-7, 8, and 9, and 11 (pulsating auroras does not reach the northward-most beam-10), It is can be seen in both Figure 3 and 5b that, N_e enhancements during pulsating auroral intervals are in general much less pronounced than during the red-line auroral intensification intervals. This result will be further reinforced with the following statistical analysis.

3.5 Statistics during quiet, pulsating aurora, and red-line aurora intervals.

In the following we shall present the core result of this study: a statistical analysis on the general behavior and altitude distribution of T_e and N_e during pulsating aurora intervals and red-

line auroral intensifications intervals. To investigate the altitude distribution, we shall collect the vertical beam and field–aligned beam data in both Freg732_v01 and WorldDay35 experiments. We shall briefly introduce the procedure we define and choose the time intervals of interest. All intervals are selected within 1145-1345 UT. The pulsating auroral interval is defined as the overall passage time of active pulsating auroras over the vertical or the field-aligned beam, which may include a successive series of individual patches. A short intermission (<1 min) between successive patch passages may at times occur within an ensemble of pulsating auroral activities, but we dismiss those short gaps due to the longer integration time (~70 sec) of PFISR long-pulse data. An easy way to check the identified pulsating auroral interval is to look into the time series of sampled THEMIS ASI counts around the beam --- the presence of pulsating aurora activity manifests as small-scale and short-period oscillations, as we have demonstrated in, e.g., Figure 3 and Figure 5a. Red-line intensification intervals are determined from the PFMSP 630 nm emission data at the elevation bin corresponding to the vertical or the field-aligned beam. In practice we use the criterion that the 630 nm intensity must feature a distinct isolated peak above 2 kR. To properly evaluate the relative enhancement of T_e and N_e associated with pulsating auroras and red-line auroral intensifications, we also need the non-intensified reference level of T_e and N_e, presumably taken during quiet auroral intervals. The existence of relatively quiet intervals amid auroral activities can be inferred from Figure 2. In practice, such quiet auroral intervals are chosen according to the PFMSP 427.8 intensity: for each quiet interval to be selected $I_{427.8}$ needs to be persistently below 3 kR for more than 5 min. We have also browsed

THEMIS ASI images to further confirm the absence of bright auroral structures passing over the beam during the selected quiet intervals. All identified intervals of quiet auroras, pulsating auroras, and red-line intensifications are listed in Table 1. Note that the identified intervals on the vertical beam and those on the field-aligned beam are understandably not the same, since the MLAT ranges corresponding to the upper F-region altitudes of the two beams are different. For example, for the pulsating auroras there are actually three separate activity intervals (see Figure 2), each passing the vertical and field-aligned beams at different time ranges. The rest of intervals within 1145-1345 UT, which are not included in any of the above three categories, are classified as the "Other" category. More specifically, the "other" category usually contains some moderate auroral activities, which are stronger than that during the quiet intervals but do not fall into the classification of "pulsating aurora" or "630 nm intensification" types.

We shall first address the overall statistics of T_e enhancements in the upper F-region. Figure 6a shows all available PFISR T_e points on vertical and field-aligned beams (after a pre-filtering procedure introduced in Section 2) during 1145-1345 UT, distinguished into four categories of auroral activities as above-depicted. One may see that the bulk of upper F-region T_e data points during pulsating auroral intervals and 630 nm intensification intervals is in general higher than that during quiet intervals. To perform a more quantitative evaluation of the increment level and statistical occurrence rate of T_e enhancements, we sample the T_e points at 420-500 km, and show their histograms corresponding to four categories of auroral activities in Figure 6b-6e. This height range is so chosen as to facilitate a direct comparison with Swarm satellite measurements

(~460 km altitude) in LJ17. The median value of each distribution as well as the lower and upper quartiles are labeled in each subfigure. It is straightforward to see that T_e during pulsating auroral intervals shows systematic enhancement over that during quiet intervals; the range of absolute T_e level and the relative T_e enhancement are both fairly comparable to that identified in LJ17. If we use 2500 K as a threshold, which is >85% percentile and >1.1 standard deviation, of the quiet-time T_e distribution, the percentage of data points with T_e >2500 K (conceived as distinguishable enhancement over quiet-time) is 88 out of 126 (~69.8%) during pulsating auroral intervals. Coincidentally, in a different context LJ17 also found that a substantial T_e enhancement is identified in ~70% of their pulsating auroral events. In a further test (not shown) we have also sampled T_e in the 300-550 km altitude range. If we similarly define the >85% percentile of quiet-time T_e at each altitude bin as the threshold of enhancement, the T_e enhancement is found in 306 out of 438 pulsating aurora T_e points --- again yielding a ratio of ~70%.

We shall then examine the altitudinal distribution of T_e . Figure 7 shows the scatter distribution of sampled T_e over altitudes for quiet auroral, pulsating auroral, and 630 nm intensification intervals. We divide F-region altitudes between 150 and 550 km into 10 bins, each separated by 40 km, and mark the median value of T_e as well as the lower and upper quartiles in those altitude bins, to facilitate readers to comprehend a general trend of the T_e profile. PFISR T_e data are obtained via ACF fitting; the color of data points in the figure denotes the ratio between the error estimate of fitting (T_{e_err}) and the fitted T_e , which may be used a semi-quantitative flag of the ACF fitting quality and data reliability. Note that in our pre-filtering procedure (see

Section 2) data with $T_{e\_err} > T_e$ have been discarded. For 75% of the data points, $T_{e\_err} < T_e /4$, so that the quality of ACF fitting is generally reasonable. Notwithstanding the spread of the data there is a clear trend of elevated T_e at altitudes >300 km during pulsating auroral intervals; the median T_e profile during quiet intervals (blue curve) is close to the lower cutoff of the T_e distribution during pulsating auroral intervals. The T_e enhancement in the altitude range ~150-250 km is however minimal. We have also checked and confirmed that the average T_{e_err} in each altitude bin above 300 km is always distinctly smaller than the separation between the median T_e during quiet intervals and that during pulsating auroral intervals in the same altitude bin. T_e is also strongly elevated during the red-line auroral intensification interval; the increment is much more evident in the lower F-region than that during pulsating auroral intervals. Another key observation lies in that, during pulsating auroral intervals the T_e distribution shows a distinguishable trend of increasing towards high altitudes. The median value of T_e, as well as its lower and upper quartiles (except at the topmost altitude bins where PFISR data quality may sometimes become questionable), increases with altitudes throughout the F-region. We have made careful statistical tests and confirmed that, the above-derived average trend of T_e profile is robust against the scatter of data during pulsating auroral intervals. This trend implies the presence of a downward heat flux, as we shall discuss in more details in Section 5. In comparison, such a trend is not as discernible during either quiet auroral intervals or red-line auroral intensification intervals.

If the observed T_e enhancements are caused by secondary electron heating, since such a heat transfer is most efficient when the energy of secondary electrons degrades to a few eV [*Rees and Jones*, 1973], just above the threshold for $O(^1D)$ excitation (~2 eV) [e.g., *Solomon et al.*, 1988], one should expect a reasonable correlation between T_e and the red-line auroral intensity. Note that in Figure 6b-6e we have marked the mean and standard deviation of the red-line auroral intensity corresponding to each category in the plot. One may see from Figure 6 that T_e is indeed superficially related to red-line auroras: it is the lowest during the quiet auroral intervals yet the highest during 630 nm intensification intervals. That said, we note that the pulsating aurora is somehow special. The red-line intensity during the "other" category intervals (representing non-pulsating moderate auroral activities) is only slightly lower than that during pulsating auroras, yet in a statistical sense the former feature substantially lower T_e level and percentage of T_e enhancement than the latter. On the other hand, the red-line auroral intensity during pulsating auroral intervals is distinctly lower than that during the 630 nm intensification intervals, yet their T_e ranges are roughly comparable.

To further check the correlation between T_e and 630 nm auroral intensity, we average T_e along the vertical or field-aligned beam at >200 km altitudes based upon PFISR data, while collecting PFMSP red-line intensity from the elevation bin corresponding to the beam direction and averaging it over the same time bin as PFISR. We exclude some PFISR time bins where the range bins with available beam T_e data is too few (<2/3 of total range bins) for us to achieve a reliable average over heights. With the above procedure, the PFMSP red-line auroral intensity

and the PFISR T_e data are sampled and integrated along the same line-of-sight path and over the same time interval. The scatter plots of the two datasets during pulsating auroral intervals and red-line intensification intervals are presented in Figure 8. The 630 nm intensity during pulsating auroral intervals is not only systematically lower than that during red-line intensification intervals, they also appear to show different correlation with T_e. For the red-line intensification intervals, there is indeed, as expected, a perceptible trend of positive correlation between T_e and 630 nm auroral intensity (R~0.63). However, for pulsating auroral intervals, the correlation between T_e and the red-line auroral intensity is insignificant, if existing at all (R~0.25). This result casts doubts on the scenario of secondary electron heating as the main underlying mechanism of the T_e enhancement during pulsating auroral intervals. We however admit that the reliability of correlation may be somehow limited by the narrower 630 nm intensity range of the pulsating aurora.

Figure 9 shows the scatter distribution of N_e over altitudes for three types of auroral intervals. We first remind that we slightly adjust the data-collecting time window of N_e statistics for some short-lived auroral activity intervals. This is because, as we have afore-noted, the N_e peak enhancement in the upper F-region might sometimes slightly lag a short-lived red-line auroral intensification. Accordingly, the N_e sampling interval is extended for up to 2 min after the end of those red-line auroral intensifications. Such adjustment is not needed for relatively long (>5 min) red-line auroral intensification and pulsating auroral intervals. Also, as shown in Figure 5b N_e enhancement somehow persists after ~1330 UT when the auroral activity decays.

We thus exclude the interval 1330-1345 UT in our sampling of quiet time N_e. Note that the pulsating aurora is known to essentially move with ambient plasma convection, so that the F-region N_e structure co-moves with the pulsating auroral flux tubes, relieving an ambiguity typical in F-region N_e variations, namely a local auroral ionization effect or a transported effect from elsewhere. As one can see, during pulsating auroral intervals the overall N_e distribution in the upper F-region does not show very discernible enhancement over that during quiet intervals: the median value of the former is moderately larger than that of the latter, but their difference is smaller than the spread of both datasets. In particular, the N_e difference between pulsating aurora and quiet intervals is fairly insignificant at ~250 km altitude and lower. In comparison, The N_e enhancement during red-line auroral intensification intervals is much more pronounced, in particular in the lower F-region where the media values increase over 100%. Such a strong N_e increment in the lower F-region is presumably mainly owing to a local ionization effect of 630 nm auroral intensifications, instead of a spatially transported effect from activities elsewhere. One may see Figure 5b for a clear example of the existence of strong N_e enhancement extending from the lower F-region to the E-region associated with the red-line auroral intensification. To summarize the above observations, while both the pulsating aurora and the red-line auroral intensification are found to be accompanied by T_e enhancements in the F-region ionosphere, their associated statistical N_e variations, as well as their levels of, and correlation with, 630 nm auroral intensities, are quite different.

Another parameter of our interest is the upward ion velocity. Figure 10 shows the scatter distribution of sampled line-of-sight velocity (VLOS) on vertical and field-aligned beams over altitudes: positive/negative values indicate upward/downward flows. We have checked the convective (perpendicular to **B**) velocity from both PFISR data and AMIE model, and inferred that the north-south convective velocity at ~66^0, roughly the center MLAT of the vertical beam in 300-500 km altitudes, is no more than a couple of hundred of m/s, either southward or northward, during the event interval. A projection of the meridional convective flows would definitely be much smaller than 100 m/s along the vertical beam, and has no effect on the field-aligned beam VLOS. As one can see, VLOS on vertical and field-aligned beams becomes dominantly upward during pulsating auroral intervals. Albeit with considerable spread, the median values of the upward flow velocity reach > 100 m/s in the upper F-region, and show an overall tendency to increase towards higher altitudes. This result indicates a nontrivial rise of ion upflows during pulsating auroral intervals. A trend of upward ion flows is also identified during red-line auroral intervals.

3.6 E-region electron heating

We shall briefly check the electron heating in the ionospheric E-region associated with pulsating auroras. The top panel of Figure 11 shows the THEMIS ASI intensity sampled on the vertical beam, with the pulsating auroral interval labeled. The 2^{nd} panel shows the long-pulse mode T_e data on the vertical beam. Evident T_e enhancements in the upper F-region exist during the pulsating aurora interval. The bottom panels shows the T_e observation form the alternating-

code (AC) mode, which is specifically designed for the E-region, of the vertical beam. The time resolution of AC mode data is ~3 min. As one can see, there are indeed clues of T_e enhancement in the altitude range ~100-120 km during the pulsating auroral interval, which is presumably led by the auroral electron precipitation. However, such T_e enhancements are not very strong, generally on order of ~100 K above the T_e values before and after the pulsating auroral interval. Given the low thermal conductivity in the E-region, it is unlikely that such a level of T_e enhancement in the E-region might cause, by way of thermal conduction, the much stronger T_e enhancement (~500-1000 K) in the upper F-region. Even one may argue that the E-region T_e enhancement might be somehow underestimated due to the long integration time of the AC mode, the observation on the minimal T_e increment (<100 K, see Figure 7b) in the transitional height range (~150-250 km) is still inconsistent with the scenario of effective heat conduction from the E-region to the upper F-region.

4. Other complementary datasets

Ionospheric electron heating is known to be subject to a number of possible source mechanisms. In this section, we shall attempt to examine some of the candidate mechanisms, within the limit of complementary datasets available during the event interval.

4.1 Characteristic energy of precipitation

At ~1305 UT, NOAA-19 satellite traverses the pulsating auroral region. In Figure 12a we plot three THEMIS ASI images with the NOAA-19 mapping overplotted, exemplifying the on and off variations of pulsating auroras. The satellite footprint is within ~2^0 MLON of the

magnetic meridian of PFISR and PFMSP during the pulsating auroral traversal. Figure 12b shows the NOAA-19 observations. The top panel shows the along-track keogram of THEMIS ASI. Such an along-track keogram is constructed by sampling and averaging image pixels within $\pm 0.2^0$ MLON around the satellite trajectory at each latitude. The second panel shows the data in the E1 channel of MEPED, which measures the high-energy (>50 keV) electron fluxes in both trapped (measured by the 90^0-telescope) and precipitating (measured by the 0^0-telescope) directions. Note that we have taken into account the correction of the effective energy range for MEPED telescope according to *Yando et al*. [2011]. Before ~1304:50 UT, the precipitating flux is in general lower than the trapped flux, indicating an empty or partially filled loss-cone. After entering the pulsating aurora, the MEPED electron fluxes increase substantially and show noticeable oscillations. At times, the precipitating flux becomes close to the trapped flux, implying a fully filled loss-cone. While the temporal resolution is different for NOAA-19 data (2 sec) and for THEMIS ASI (3 sec), one may still marginally view the similarity between the on-off variation of the pulsating aurora and the oscillation of the precipitating flux, e.g., at around 1305:06 UT (see Figure 11a). In comparison, the TED electron flux in the energy range (1-20 kV) does not show very noticeable variations upon entering the pulsating aurora. Such a comparison hints that a substantial portion of the pulsating auroral precipitation is likely beyond the TED energy range, e.g., > 20 keV. The 50-1000 eV electron flux is very small during the traversal, implying that there is no appreciable presence of soft electron precipitation on order of hundreds of eV for the pulsating aurora. We have further checked the TED flux at its lowest

sampled energy bin 154-224 eV, and found the flux very low during the pulsating auroral traversal, further excluding the existence of ~100 eV electron precipitation with this pulsating aurora.

The 4th panel of Figure 12b shows the energy bin where the differential flux maximizes within the full energy range of TED (50 eV-20 keV) at each data record epoch. Max-flux energy bins of both sensors of TED (0^0 and 30^0 view angle) are shown, but they are identical during the pulsating auroral traversal of interest. Such a max-flux energy is often used to infer the characteristic energy of precipitation, but in our event we note that, since the differential fluxes persistently maximize at the topmost energy bin of TED (14-20 keV centering at 17 keV) during the pulsating auroral traversal, it is quite possible that the actual characteristic energy of precipitation might be even higher than 20 keV. To conclude, inferred from the NOAA-19 TED and MEPED data, it is almost certain that a major portion of the pulsating auroral precipitation is contributed by high-energy ($\geq$ 20 keV) electrons.

The bottom panel of Figure 12b shows the precipitation flux of low-energy ions (50 eV-1 keV). There is an enhancement of low-energy ion precipitation flux accompanying the pulsating auroral traversal. This was found to be a common feature of pulsating auroras [*Liang et al.*, 2015]. Such a low-energy ion precipitation structure alludes to the existence of low-energy plasma flux tubes threading the pulsating aurora, a hypothesis of crucial importance to this study, as we shall discuss in details in Section 4.

The intensity ratios among different auroral emission lines have long been used in inferring the characteristic energy of auroral precipitation [e.g., *Rees and Luckey*, 1974; *Jones et al.*, 1987]. In general, the lower the ratio between the 557.7 nm or 630 nm intensity to the 427.8 nm intensity, the higher the characteristic energy of precipitation. In this regard, we sample the PFMSP 427.8 nm, 557.7 nm, and 630 nm intensities along the vertical or field-aligned beam, during the passage of pulsating auroras over the corresponding beam (see Table 1). The scatter plots of these sampled intensities are given in a supplementary material (Figure S1). To evaluate the green-to-blue ratio, we apply two different approaches. The first is a linear fit between the two emission intensities, which yields $I_{557.7} = 1.54 \cdot I_{427.8} + 2155$, and the other is via direct statistics of the green-to-blue ratio, $I_{557.7} / I_{427.8} = 1.89 \pm 0.14$. The ratios inferred from the two ways are understandably different, since the pulsating aurora is known to be embedded in ambient diffuse auroras, the latter of which may have lower characteristic energy of precipitation and thus higher green-to-blue ratio. The actual green-to-blue ratio corresponding to the pulsating auroral component is probably somewhere between ~1.6 and ~1.8. Similarly we also check the ratio between 630 nm intensity and 427.8 nm intensity with the above procedure, and estimate a red-to-blue ratio of order of ~0.1 for the pulsating auroral component. The above ratios would point to a characteristic energy of >10 keV, based upon a lookup in the existing literature (e.g., *Jones et al.* [1987]), and an evaluation from our model [*Liang et al.*, 2016] within reasonable range of the atmospheric O/N_2 content ratio (~0.2-0.8, see e.g., *Hecht et al.* [2008]). Admittedly, the above evaluation is limited by the assumption of single-Maxwellian distribution of the primary

electron precipitation, but the result is nevertheless consistent with the NOAA-19 observations in that, they both reveal that a main portion of the pulsating auroral precipitation lies above 10 keV. This is in line with the common understanding and observations of the pulsating auroral precipitation [*Sandahl et al*., 1980; *Jones et al*., 2009; *Nishimura et al*., 2011; *Lessard*, 2012; *Jaynes et al*., 2013; *Miyoshi et al*., 2015; *Samara et al*., 2015; *Oyama et al*., 2017]. Based upon known properties of secondary electron heating, such a high-energy electron precipitation is unlikely to adequately account for the observed strong T_e enhancement in the upper F-region.

4.2 On the electron/ion temperature ratio and anomalous electron heating

Anomalous electron heating at upper ionospheric altitudes is known to be capable of producing strong electron heating there [e.g., *Forme et al*., 1993]. Candidate instability modes that may contribute to anomalous electron heating include the ion acoustic and the ion cyclotron instabilities. The ratio between T_e and T_i is one of the key factors controlling the threshold of the above instabilities [*Kindel and Kennel*, 1971; *Forme et al*., 1993]. We infer from the PFISR data that, the T_e/T_i ratio during the interval of interest is almost exclusively within the range ~1-3. Assuming a FAC of ~1 $\mu A/m^2$, the mean value within pulsating auroras as surveyed in LJ17, we find that the threshold for either the ion acoustic or the ion cyclotron instabilities is remotely unreachable. It is thus unlikely that anomalous electron heating might operate locally as the underlying mechanism of the observed T_e enhancement.

4.3 On the FAC intensity

The field-aligned motion of ionospheric thermal electrons, which carries at least part of the FAC, may also play a role in modifying the T_e profile in the ionosphere [e.g., *Abe et al*., 1993; *Zhang et al*., 2003]. As can be inferred from *Zhang et al*. [2003] as well as from our numerical test with LJ17 model, to produce a T_e enhancement > 500 K in the upper F-region, an upward FAC of the order of 10 $\mu A/m^2$ or higher is required. However, via a Swarm survey LJ17 found that the upward FAC magnitude averaged over the pulsating auroral patch is typically on order of ~1 $\mu A/m^2$. There is no direct and instantaneous measurement of FAC in our event, let alone distinguishing the FAC component carried by ionospheric thermal electrons and that carried by precipitating auroral electrons. We may only perform a gross overview of the large-scale FAC intensity during pulsating auroral intervals. During 1220-1230 UT, when pulsating auroras are active over PFISR, one of the meridional constellation of Iridium satellites is very close to the Poker Flat meridian (see Figure S2 in supplementary material). The FAC along the Poker Flat meridian calculated via the AMPERE analysis is shown in Figure S2c. For the pulsating auroras that exist around and extend slightly poleward of Poker Flat, where PFISR measurements are from, their corresponding FAC intensity is relatively small (<0.2 $\mu A/m^2$) and/or in a transition from upward to downward FACs. We also use the AMIE technique [*Richmond and Kamide*, 1988] to estimate the large-scale FAC. Figure S2d-S2i present six frames of AMIE maps, each with 2-min integration time, selected from three time intervals when pulsating auroras are active over PFISR. Upon browsing the AMIE results during all pulsating auroral intervals of interest, we notice that PFISR also appears to be situated in a transition from Region-1 (downward) FACs

to Region-2 (upward) FACs. To summarize, while admittedly the temporal and spatial resolution of AMPERE and AMIE data are non-ideal, based upon existing datasets we may at least exclude the existence of strong enough (>> 1 $\mu A/m^2$) upward FACs, in a large-scale and average sense, that might contribute substantially to the observed T_e enhancement in the upper F-region ionosphere during pulsating auroral intervals. Small-scale and transient FACs associated with individual auroral patches are not resolvable in the current study.

5. Discussions

We have used joint optical and PFISR observations to study the ionospheric plasma signatures related to pulsating auroras. Consistent with the results in our previous study LJ17 using Swarm satellite survey, we again identify strong electron heating in the upper F-region associated with pulsating auroras. The combination of multi-wavelength auroral observations and radar measurements in this study lays a solid ground for us to explore the underlying mechanism of the electron heating, as we shall unfold in this section. We shall first put forth a caveat that, we are not claiming a strictly one-to-one correspondence between each pulsating aurora patch and the T_e enhancement, which is not the case as shown in LJ17. Admittedly, data error/uncertainties aside, the considerable spread shown in our statistics implies that the ionospheric variations associated with pulsating auroras might be complicated; the underlying mechanisms for both pulsating auroras and their ionospheric effects could be variable.

Nevertheless, a statistical majority of T_e enhancement during pulsating auroral intervals is incontrovertible in both LJ17 and in this study. When we proceed in our following discussions on the variation trend and profile of T_e and N_e during pulsating auroral intervals, we mean those in a general and statistical sense, and our goal is to explore the main underlying mechanism that might exist and operate in a majority of pulsating auroral events. Complication and exception certainly may exist, and shall be kept in mind throughout the reading.

One of the main uncertainties in LJ17 lies in that, we may not totally exclude the possibility that the Swarm-observed T_e enhancement could be a thermal conduction effect from the lower ionosphere, due to extremely strong electron heating in the E-region, which is not impossible in the presence of anomalous heating [e.g., *Schlegel and St. Maurice*, 1981]. With the aid of PFISR data in this study, the above possibility is excluded. The T_e enhancement (~100 K) in the E-region accompanying the pulsating aurora is nontrivial yet not extraordinarily strong, and the T_e increment at the transitional height (~150-200 km) from E-region to F-region is even smaller (< 100 K). It is thus unlikely that the strong electron heating in the upper F-region is led by thermal conduction from the lower E-region ionosphere. The presence of local anomalous heating in the upper F-region is not supported either: according to the observed T_e/T_i ratio, the threshold of plasma instabilities that are known to be conductive to anomalous heating is unreachable.

We have collected and compared PFISR data during pulsating auroral intervals and red-line auroral intensification intervals, and notice that, while the two classes of auroral activities are both associated with T_e and N_e enhancements, they differ in a number of aspects:

(1) There are substantial T_e enhancements in the upper F-region during pulsating auroral intervals. The overall statistical T_e profile shows a distinguishable trend of increasing towards high altitudes. On the other hand, during red-line auroral intensifications, while the T_e enhancement is stronger in the lower F-region than that during pulsating auroral intervals, there is no perceptible trend of increasing T_e with altitudes.

(2) The N_e enhancement is systematically smaller during the pulsating auroral intervals than that during the red-line intensification intervals; the discrepancy is particularly pronounced in the lower F-region where the N_e enhancement maximizes during red-line intensifications.

(3) The 630 nm auroral intensity is distinctly lower, and shows little correlation with T_e during pulsating auroral intervals, while there is a reasonable correlation between T_e and 630 nm intensity during red-line auroral intensification intervals.

The above observations and comparisons lead us to conceive that the T_e enhancements during the two classes of auroral activity may be attributed to fundamentally different mechanisms. For the red-line auroral intensification, the underlying mechanism of T_e enhancement appears to be straightforward: secondary electron heating. Note that the presence of red-line auroral intensification itself indicates a substantial level of secondary electron fluxes in the F-region ionosphere. Since the energy threshold for O(^1D) excitation is ~2 eV, close to the energy level of secondary electrons that are most effective in transferring heat to ionospheric thermal electrons [*Rees and Jones*, 1973], a correlation between T_e and the red-line auroral

emission is expected, and is indeed evidenced in Figure 8b. For electron precipitation with characteristic energy above a few hundred eV, the secondary electron flux and its resultant impact ionization would produce strong N_e enhancement that extends from F-region to E-region, as seen in Figure 5b and Figure 9c. We thus propose that the T_e and N_e enhancement during the red-line auroral intensification is basically consistent with the secondary electron heating/ionization scenario.

The major mechanism underlying the upper F-region T_e enhancement during pulsating auroral intervals is somehow puzzling. The secondary electron heating mechanism in the F-region is contingent upon the characteristic energy of precipitation: the higher the characteristic energy of the primary precipitation, the lower altitudes it can penetrate to, and the less heating effect it yields at higher altitudes. We have evaluated from both optical auroral data and NOAA-19 measurements that, the pulsating auroras of interest likely mainly consist of high-energy (>10 keV) electron precipitation. The secondary electron heating is thus not supposed to be effective in the upper F-region. To be more quantitative, we perform a simulation using the model described in LJ17. We use the location of Poker Flat, the event date and time (19 March 2015 13 UT), and the F10.7 and AP index corresponding to the event interval, as inputs to the model. For the quiet aurora, presumably corresponding to ambient diffuse aurora, we assume a Maxwellian precipitation flux spectrum with characteristic energy of 2 keV and total flux of 2 erg/cm^2/s, for the pulsating auroral precipitation we add another Maxwellian flux spectrum with characteristic energy of 20 keV and an energy flux of 8 erg/cm^2/s. The two components add up to a total

energy flux of ~2.6 erg/cm2/s in the 1-20 keV energy range, ~0.028 erg/cm^2/s in the 50-1k eV energy range, and a directional number flux of ~1.1 × 10^7/cm^2/s/sr in >50 keV energy range; they are all compatible with, yet close to the upper-limit of, the actual NOAA-19 TED and MEPED measurements during the pulsating auroral traversal (see Figure 12b). We assume the ionospheric electron thermal FAC to be 0 for the quiet aurora and 1 μA/m^2 for the pulsating aurora, and the same heat flux 2 × 10^9 eV/cm^2/s at the upper boundary of ionosphere for both runs. The simulation outcome is shown in Figure 13. The blue curve denotes the T_e profile corresponding to the quiet aurora, and the black curve indicates T_e with the inclusion of energetic electron precipitation characteristic of the pulsating aurora. As one can see, the addition of the energetic electron precipitation, together with a level of 1 μA/m^2 upward FAC, lead to a T_e enhancement of only several tens of K in the upper F-region. This result largely excludes the possibility that secondary electron heating led by energetic electron precipitation serves as the major and statistically prevalent mechanism of the observed T_e enhancement in the upper F-region ionosphere, though we do not deny its partial (or occasionally major) role. Furthermore, Figure 8a indicates that T_e shows little discernible correlation with the red-line intensity during pulsating auroral intervals. This also suggests that the observed T_e enhancement associated with the pulsating auroral activity may not be statistically related to secondary electron fluxes led by the energetic electron precipitation.

The solution to the above dilemma lies in that, the energetic electron precipitation is not the only module involved in the pulsating auroral phenomenon. In terms of the auroral excitation,

the pulsating aurora and its ambient diffuse aurora can often be grossly attributed to the energetic (suprathermal) and thermal population of electrons in the central plasma sheet (CPS), respectively [e.g., *Nishimura et al*., 2011; *Lessard*, 2012]. However, it has long been realized that the spatial characteristics of pulsating auroras, namely what processes define the shape/size of the patch, cannot be accounted for by CPS energetic or thermal particles. It is established that the motion of the pulsating auroral patch essentially conforms to the E×B convection drift [*Scourfield et al.*, 1983; *Yang et al*., 2015; 2017]. Also, individual patches can often maintain their rough shape and size over many sequences of luminosity pulsations. Energetic or thermal particles undergo curvature/gradient drifts in the near-Earth CPS. Their motion may deviate substantially from the E×B convection, and their structural shape is subject to rapid deformation and dispersion due to energy-dependent drifts over a time span of no more than a couple of minutes.

Bases upon the above rationale, it has long been hypothesized that the pulsating aurora patch might connect to magnetospheric flux tubes filled with enhanced "cold" plasma [*Johnstone*, 1978; *Davidson*, 1990; *Demekhov and Trakhtengerts*, 1994]. Such cold plasma may form an ambient structure that can significantly affect the excitation and propagation of ELF/VLF waves and their interaction with energetic electrons within the cold-plasma flux tubes [*Li et al*., 2011; *Wu et al*., 2013; *Katoh*, 2014]. So far there is still a lack of definite observations on the magnetospheric cold plasma structure tied to the pulsating aurora, yet several indirect clues existed in the literature [*Nishiyama et al*., 2012; *Liang et al*., 2015; *Nishimura et al*., 2015].

Liang et al. [2015] surveyed pulsating auroral events when low-Earth-orbit satellites traversed pulsating aurora patches, and found in a majority of events the existence of a low-energy ion precipitation structure (LEIPS) that is collocated with the patch. Such a LEIPS associated with the pulsating aurora is also observed by NOAA-19 in this study (see the bottom panel of Figure 12b). *Nishimura et al*. [2015] proposed that fluctuations of LEIPS density can modulate the growth of whistler-mode chorus and in turn the pitch-angle scattering of energetic electrons in the CPS, potentially leading to pulsating auroras. Considering the requirement of charge balance and the fact that the pulsating aurora is usually associated with limited FAC intensity [*Gillies et al*., 2015; LJ17], the energy range of the magnetospheric cold electrons flowing in pulsating auroral flux tubes is presumably much lower than that of the LEIPS, possibly lower than the satellite potential (see relevant arguments in *Nishimura et al*. [2015]). This is likely the reason for the lack of direct satellite observations on cold electron structures tied to pulsating auroral flux tubes in the existing literature.

Such magnetospheric cold electrons cannot penetrate into the ionosphere, but their induced heat flux may be remotely sensed in the F-region ionosphere. We suggest that PFISR T_e observations might offer another indirect clue on the possible existence of low-energy electrons on top of the ionosphere associated with pulsating auroras. As we have noted with Figure 7b, the T_e profile in the upper F-region generally shows an increasing trend toward high altitude during pulsating auroral intervals. This points to a downward heat flux. The definition of heat flux is:

$$q_{e//} = -\beta_e j_{//} - K_{\mathbf{e}} \cdot \nabla_{//} T_e \quad . \tag{2}$$

We ignore the thermoelectric term (the first term on the right-hand-side of equation) which is usually much smaller than the thermal conduction term (the second term). In the upper F-region and the topside ionosphere, a good approximation of the electron thermal conductivity is given by [*Rees and Nobel*, 1975; *Schunk and Nagy*, 1978]: $K_e \approx 7.7\times10^5 T_e^{5/2}$ eVcm^{-1}s^{-1} . Therefore, the heat flux can be simplified as,

$$q_e \approx -2.2\times10^5 \sin I \cdot \frac{d}{dz}\left(T_e^{7/2}\right) \text{ eV/cm}^2\text{/s} \quad , \tag{3}$$

where I is the magnetic inclination angle (~78^0 in our case). Negative value of q_e indicates a downward heat flux. A linear regression of sampled T_e data at >350 km altitudes in Figure 7b yields $T_e^{7/2} \sim -1.28\times10^{12} + 6.02\times10^4 \cdot z$ (z is in unit of cm and T_e is in unit of K). We thus deduce an estimate of the average downward heat flux of ~1.29 × 10^{10} eV/cm^2/s. We also test to perform the regression with T_e fitting error considered, and obtain a heat flux a ~7.96 × 10^9 eV/cm^2/s . These levels are within the attainable range of topside heat fluxes reported in the existing literature, but is higher than the statistical mean (representing the typical ambient value) of heat fluxes in the midnight-postmidnight ionosphere, which is typically at most a couple of 10^9 eV/cm^2/s [e.g., *Evans*, 1973; *Blelly and Alcayde*, 1994; *Fallen and Watkins*, 2013]. Such a downward heat flux is presumably conducted from the topside ionosphere. To check the effective role of the topside heat flux, we re-run the previous model simulation with a heat flux of 1 × 10^{10} eV/cm^2/s imposed at the upper boundary of the ionosphere. As one can see in Figure 13, T_e increases by several hundred up to ~1000 K in the upper F-region, consistent with the

observed level of T_e enhancements during pulsating auroral intervals. The model simulation thus supports the hypothesized presence of topside heat flux and its crucial role on the electron heating in the F-region ionosphere. If one recalls the nature of the heat flux (see the Introduction section), the origin of the heat flux near the topside boundary of the ionosphere is likely led by the incidence of magnetospheric low-energy electrons. Under such a notion, the existence of substantial downward heat flux can be deemed as indirect evidence of the presence of low-energy plasma on top of the ionosphere in association with the pulsating aurora. The low-energy magnetospheric plasma, the heat flux, and the pulsating auroral patch are threaded in the same flux tubes and all together essentially co-move with the E×B convection drift, such that the electron heating in the F-region ionosphere would be tied to, and co-move with, the pulsating aurora. We however remind that, inferred from *Nishiyama et al*. [2011] the cold plasma density in pulsating auroral flux tubes has substantial variability, so that the corresponding heat flux also presumably varies from case to case. This possibly explains the fact that not all pulsating auroral patches are found to be accompanied by noticeable T_e enhancements, as revealed in LJ17 and this study.

One may notice the similarity between our proposed heating mechanism and that established for the stable auroral red (SAR) arcs in the subauroral ionosphere [*Roble and Reses*, 1975; *Kozyra et al.,* 1990; *Fok et al.,* 1991]. During geomagnetically disturbed times, cold plasmaspheric electrons can be heated, e.g., via Coulomb collisions with ring current ions [*Kozyra et al.,* 1987; *Fok et al*., 1993], and become suprathermal. These suprathermal

plasmaspheric electrons may bring strong heat flux into the topside ionosphere and elevate the upper F-region T_e , leading to thermal excitation of 630 nm emissions known as SAR. For pulsating auroras, we suggest that the T_e heating mechanism might be similar to that in SAR, though the thermal excitation of red-line emissions is presumably overwhelmed by that led by the auroral precipitation.

We summarize in Table 2 the respective role and effect of energetic and low-energy electrons from the magnetosphere, two indispensable components of the pulsating aurora, in different altitude regions of the ionosphere. In a nutshell, energetic electrons deposit most of their energy at lower altitudes, where they excite the auroral emission, yet contribute trivially to electron heating in the upper F-region. The magnetospheric structure of low-energy plasma controls the shape and motion of the pulsating auroral patch. Upon precipitating onto the ionosphere, the low-energy magnetospheric electrons collide with and transfer heat to topside ionospheric electrons, leading to a heat flux, which will be conducted downward to the F-region ionosphere and elevate T_e there. The occurrence and level of the F-region T_e enhancement are contingent upon the strength of the heat flux. However, we admit that, within available observations we cannot exclude another possibility that the heat flux may stem from the auroral acceleration region [*Forme et al*, 1993], where in certain cases was suggested as the origin of pulsating auroras [e.g., *Sato et al*., 2004].

The other meaningful result of this study is the trend of enhanced ion upflows during pulsating auroral intervals. Ion outflows are common phenomena in the high-latitude ionosphere,

and may play important roles in magnetospheric dynamics and magnetospheric-ionosphere coupling processes. For outflows to occur, ions have to be lifted up (aka "upflows") first by an ambipolar electric field to the topside ionospheric altitudes, where they are then further accelerated by other processes such as wave heating to escape the Earth. Two major driving mechanisms of ion upflows are commonly recognized, namely the ion fractional heating and the soft electron precipitation [e.g., *Strangeway et al*., 2005; *Burchill et al*., 2010]. In this study, we raise another potential mechanism that may cause ion upflows, namely the strong electron heating associated with the pulsating aurora. It is well known that, the change of ionospheric T_e profile may modify the electron scale height and give rise to an ambipolar electric field that leads to ion upflows [*Strangeway et al*., 2005]. Note that the plasma outflows were hypothesized as one possible origin of the low-energy plasma in pulsating auroral flux tubes [*Liang et al*., 2015; *Nishimura et al*. 2015], so that our above proposal may constitute a self-consistent feedback loop for pulsating auroras (see Figure 9 in *Nishimura et al*. [2015]).

6. Summary and conclusion

This study built upon the work done in the previous study LJ17, using collocated optical and PFISR ISR observations to further investigate the variations of ionospheric plasma parameters associated with pulsating auroras. In an event occurring on 19 March, 2015, we identify a statistical trend of strong T_e enhancements (~500-1000 K) in the upper F-region ionosphere during the passages of pulsating auroras over PFISR, though the correspondence between T_e

enhancements and individual pulsating patches may not be one-to-one. Using multi-instrument observations we examined the possible underlying mechanisms of the observed electron heating associated with pulsating auroras. Our analysis procedure and conclusions are summarized as follows.

1. The pulsating auroras and 630 nm auroral intensifications feature a similar level of T_e enhancements in the upper F-region, but their associated N_e and red-line auroral intensities are distinctly different. For pulsating auroras, (a) T_e shows little discernible correlation with the red-line auroral intensity; (b) there is no well-discernible and repeatable N_e enhancements in the F-region ionosphere. In contrast, for 630 nm intensifications, (a) there is a reasonable correlation between T_e and the red-line auroral intensity; (b) much stronger N_e enhancement is found during 630 nm intensification intervals, particularly in the lower F-region. The above comparisons lead us to suggest that, the 630 nm intensifications are consistent with the scenario of soft electron precipitation and/or the secondary electron heating/ionization, while the pulsating auroras are in general not. Furthermore, inferred from POES/NOAA satellite and PFMSP observations, pulsating auroras are mainly composed of energetic electron precipitation with characteristic energy >10 keV, which is inefficient in secondary electron heating in the upper F-region. Based upon the above observations we propose that the secondary electron heating might not be the main mechanism contributing to the observed T_e enhancement during pulsating auroral intervals.

2. We exclude the thermal conduction from the E-region ionosphere as a viable mechanism, via checking the PFISR AC mode data in the E-region and the T_e enhancement in the transition altitudes (~150-200 km) from E- to F-region.

3. We exclude the local operation of anomalous heating in the upper F-region, since the observed T_e/T_i ratio is far smaller than the threshold for plasma instabilities that are known to cause anomalous heating.

4. We infer the existence of substantial downward heat fluxes in the upper ionosphere based upon the following observations and simulations. (a) The T_e profile in the upper F-region statistically shows an increasing trend toward high altitudes during pulsating auroral intervals; a downward heat flux of the order of ~1×10^{10} eV/cm^2/s is deduced. (b) Model simulation results indicate that such a level of heat flux is capable of producing the observed T_e enhancement in the upper F-region ionosphere during pulsating auroral intervals.

Combining the previous study, LJ17, which used Swarm satellite data and model simulations, with the PFISR and optical observations presented in the current study, we conclude that the observed T_e enhancement associated with pulsating auroras is, in a statistical sense, consistent with the topside heat flux conduction scenario. In such a scenario, the topside ionosphere electrons are heated via collisions with low-energy electrons from the magnetosphere, and the heat is conducted toward lower altitudes into the F-region ionosphere. Such a heating mechanism is similar to what is known to contribute to SAR in the storm-time

subauroral ionosphere. The above scenario is consistent with the long-hypothesized feature of pulsating auroras, namely the coexistence of a low-energy plasma population in addition to the energetic pulsating auroral precipitation, in magnetospheric flux tubes threading the pulsating auroral patch.

A trend of enhanced ion upflows during pulsating auroral intervals was also identified. We propose that the strong T_e enhancement in the upper F-region may change the electron scale height, hereby giving rise to an ambipolar electric field that drives ion upflows.

Acknowledgement. PFISR is operated by SRI International under NSF Cooperative Agreement AGS-1133009, and PFISR data is available through the Madrigal Database (http://isr.sri.com/madrigal). The Meridian Spectrograph operations are supported by NSF cooperative agreement AGS-1133009 and NASA support for Poker Flat operations. Spectrograph data are available at optics.gi.alaska.edu/optics/archive. The THEMIS mission is supported by NASA. Funding for the THEMIS ASI operation is provided by the CSA. THEMIS ASI data can be obtained via the University of Calgary data portal at http://data-portal.phys.ucalgary.ca/. POES is launched and supported by NOAA. POES data are obtained via NOAA data center ftp://satdat.ngdc.noaa.gov/sem/goes/data/.

References

Abe, T., K.-I. Oyama, S. Watanabe, and H. Fukunishi, Characteristic features of electron temperature and density variation in field-aligned current regions, J. Geophys. Res., 98, 11,257– 11,266, 1993.

Bekerat, H. A., R. W. Schunk, *and* L. Scherliess *(*2007*)*, Estimation of the high-latitude topside electron heat flux using DMSP plasma density measurements, J. Atmos. Sol.-Terr. Phys., 69*(*9*)*, 1029–1048.

Blelly, P.-L., and D. Alcayde (1994*)*, Electron heat flow in the auroral ionosphere inferred from EISCAT-VHF observations, J. Geophys. Res., 99*(*A7*)*, 13,181–13,188, *doi:*10.1029/93JA03493.

Burchill, J. K., D. J. Knudsen, J. H. Clemmons, K. Oksavik, R. F. Pfaff, C. T. Steigies, A. W. Yau, and T. K. Yeoman (2010), Thermal ion upflow in the cusp ionosphere and its dependence on soft electron energy flux, J. Geophys. Res., 115, A05206.

David, M., R. W. Schunk, and J. J. Sojka (2001), The effect of downward electron heat flow and electron cooling processes in the high-latitude ionosphere, J. Atmos. Sol. Terr. Phys, 73, 1029-1048.

Davidson, G. T. (1990), Pitch-angle diffusion and the origin of temporal and spatial structures in morningside aurorae, Space Sci. Rev, 53, Issue 1-2, 45-82.

Demekhov, A. G., and V. Y. Trakhtengerts (1994), A mechanism of formation of pulsating aurorae, J. Geophys. Res., 99(A4), 5831–5841, doi:10.1029/93JA01804.

Donovan, E. F., et al. (2006), The THEMIS all-sky imaging array—system design and initial results from the prototype imager, J. Atmos. Sol. Terr. Phys, 68, 1472–1487.

Evans, J. V. (1973), Millstone Hill Thomson scatter results for 1966 and 1967, Planet. Space Sci., 21(5), 763–792, doi:10.1016/0032-0633(73)90095-0.

Fallen, C. T., and B. J. Watkins *(*2013*)*, Diurnal and seasonal variation of electron heat flux measured with the Poker Flat Incoherent-Scatter Radar, J. Geophys. Res. Space Physics, 118, 5327–5332, *doi:*10.1002/jgra.50485.

Fok, M.-C., J. U. Kozyra, M. F. Warren, and L. H. Brace (1991), Seasonal variations in the subauroral electron temperature enhancement, J. Geophys. Res., 96(A6), 9773–9780, doi:10.1029/91JA00791.

Fok, M.-C., J. U. Kozyra, A. F. Nagy, C. E. Rasmussen, and G. V. Khazanov (1993), Decay of equatorial ring current ions and associated aeronomical consequences, *J. Geophys. Res.*, 98(A11), 19381–19393, doi:10.1029/93JA01848.

Forme, F., Wahlund, J.-E., Opgenoorth, M. Persson, and E. V. Mishin (1993), Effects of current driven instabilities on the ion and electron temperatures in the topside ionosphere, J. Atmos. Terr. Phys. 55(4), 647–666.

Gillies, D. M., D. Knudsen, E. Spanswick, E. Donovan, J. Burchill, *and* M. Patrick *(*2015*)*, Swarm observations of field-aligned currents associated with pulsating auroral patches, J. Geophys. Res. Space Physics, 120, 9484–9499, *doi:*10.1002/2015JA021416.

Grono, E., E. Donovan, and K. R. Murphy, Tracking patchy pulsating aurora through all-sky imagers, Ann. Geophys, 35, 777-784, 2017.

Hecht, J. H., et al. (2008), Satellite and ground-based observations of auroral energy deposition and the effects on thermospheric composition during large geomagnetic storms: 1. Great geomagnetic storm of 20 November 2003, J. Geophys. Res., 113, A01310, doi: 10.1029/2007JA012365.

Hosokawa, K., Y. Ogawa, A. Kadokura, H. Miyaoka, *and* N. Sato *(*2010*)*, Modulation of ionospheric conductance and electric field associated with pulsating aurora, J. Geophys. Res., 115*, A03201, doi:*10.1029/2009JA014683.

Hosokawa, K., and Y. Ogawa (2015), Ionospheric variation during pulsating aurora, J. Geophys. Res. Space Physics, 120, 5943–5957, doi:10.1002/2015JA021401.

Jaynes, A. N., M. R. Lessard, J. V. Rodriguez, E. Donovan, T. M. Loto'aniu, *and* K. Rychert *(*2013*)*, Pulsating auroral electron flux modulations in the equatorial magnetosphere, J. Geophys. Res., 118, 4884–4894, *doi:*10.1002/jgra.50434.

Johnstone, A. D. (1978), Pulsating aurora, Nature, vol. 274, 119-126.

Jones, A. V., R. L. Gattinger, P. Shih, J. W. Meriwether, V. B. Wickwar, and J. Kelly *(*1987*)*, Optical and radar characterization of a short-lived auroral event at high latitude, J. Geophys. Res., 92*(*A5*)*, 4575–4589, *doi:*10.1029/JA092iA05p04575..

Jones, S. L., et al. (2009), PFISR and ROPA observations of pulsating aurora, J. Atmos. Sol. Terr. Phys., 71, 708, doi:10.1016/j.jastp.2008.10.004.

Katoh, Y. (2014), A simulation study of the propagation of whistler-mode chorus in the Earth's inner magnetosphere, *Earth, Planets and Space*, **66**:6.

Kindel, J. M., *and* C. F. Kennel *(*1971*)*, Topside current instabilities, J. Geophys. Res., *76(*13*)*, 3055–3078, *doi:*10.1029/JA076i013p03055.

Kozyra, J. U., E. G. Shelley, R. H. Comfort, L. H. Brace, T. E. Cravens, A. F. Nagy, The role of ting current O^+ in the formation of stable auroral red arcs, *J. Geophys. Res.*, **92**, 7487–7502, 1987.

Kozyra, J. U., C. E. Valladares, H. C. Carlson, M. J. Buonsanto, and D. W. Slater (1990), A theoretical study of the seasonal and solar cycle variations of stable aurora red arcs, J. Geophys. Res., 95(A8), 12219–12234, doi:10.1029/JA095iA08p12219.

Lessard, M. R. (2012), A Review of Pulsating Aurora, in Auroral Phenomenology and Magnetospheric Processes: Earth And Other Planets (eds A. Keiling, E. Donovan, F. Bagenal and T. Karlsson), American Geophysical Union, Washington, D. C. doi: 10.1029/ 2011GM001187.

Li, W., J. Bortnik, R. M. Thorne, Y. Nishimura, V. Angelopoulos, and L. Chen (2011), Modulation of whistler mode chorus waves: 2. Role of density variations, J. Geophys. Res., 116, A06206, doi:10.1029/2010JA016313.

Liang, J., E. Donovan, Y. Nishimura, B. Yang, E. Spanswick, K. Asamura, T. Sakanoi, D. Evans, and R. Redmon (2015), Low-energy ion precipitation structures associated with pulsating auroral patches, J. Geophys. Res. Space Physics, 120, 5408–5431, *doi:* 10.1002/2015JA021094.

Liang, J., E. Donovan, B. Jackel, E. Spanswick, *and* M. Gillies (2016), On the 630 nm red-line pulsating aurora: Red-line Emission Geospace Observatory observations and model simulations, J. Geophys. Res. Space Physics, 121, 7988–8012, *doi:*10.1002/2016JA022901.

Liang J., B. Yang, E. Donovan, J. Burchill, and D. Knudsen (2017), Ionospheric electron heating associated with pulsating auroras: A Swarm survey and model simulation, J. Geophys. Res. Space Physics, 122, 8781–8807, doi:10.1002/2017JA024127.

Miyoshi, Y., et al. (2015), Energetic electron precipitation associated with pulsating aurora: EISCAT and Van Allen Probe observations. J. Geophys. Res. Space Physics, 120, 2754–2766, *doi:* 10.1002/2014JA020690.

Nishimura, Y., et al. (2011), Multievent study of the correlation between pulsating aurora and whistler mode chorus emissions, J. Geophys. Res., 116, A11221, doi:10.1029/ 2011JA016876.

Nishimura, Y., J. Bortnik, W. Li, J. Liang, R. M. Thorne, V. Angelopoulos, O. Le Contel, U. Auster, *and* J. W. Bonnell (2015), Chorus intensity modulation driven by time-varying field-aligned low-energy plasma, J. Geophys. Res. Space Physics, 120, 7433–7446, *doi:*10.1002/2015JA021330.

Nishiyama, T., T. Sakanoi, Y. Miyoshi, Y. Katoh, K. Asamura, S. Okano, and M. Hirahara (2011), The source region and its characteristic of pulsating aurora based on the Reimei observations, J. Geophys. Res., 116, A03226, doi:10.1029/2010JA015507.

Oyama, S., Y. Miyoshi, K. Shiokawa, J. Kurihara, T. T. Tsuda, and B. J. Watkins (2014), Height-dependent ionospheric variations in the vicinity of nightside poleward expanding aurora after substorm onset, J. Geophys. Res. Space Physics, 119, 4146–4156, doi:10.1002/ 2013JA019704.

Oyama, S., et al. (2017), Energetic electron precipitation and auroral morphology at the substorm recovery phase, J. Geophys. Res. Space Physics, 122, 6508–6527, doi: 10.1002/2016JA023484

Rees, M. H., and R. A. Jones (1973), Time dependent studies of the aurora, 2, Spectroscopic morphology, Planet. Space Sci., 22, 1213.

Rees, M. H., and R. G. Roble (1975), Observations and theory of the formation of stable auroral red arcs, Rev. Geophys., 13(1), 201–242, doi:10.1029/RG013i001p00201.

Rees, M., and D. Luckey (1974), Auroral Electron Energy Derived From Ratio of Spectroscopic Emissions, 1. Model Computations, J. Geophys. Res., 79(34), 5181-5186.

Royrvik, O., and T. N. Davis (1977), Pulsating Aurora: Local and Global Morphology, J. Geophys. Res., 82(29), 4720–4740.

Samara, M., R. G. Michell, *and* R. J. Redmon *(*2015*)*, Low-altitude satellite measurements of pulsating auroral electrons, J. Geophys. Res. Space Physics, 120, 8111–8124, *doi:*10.1002/2015JA021292.

Sandahl, I., L. Eliasson, *and* R. Lundin *(*1980*),* Rocket observations of precipitating electrons over a pulsating aurora, Geophys. Res. Lett., 7, 309–312, *doi:*10.1029/GL007i005p00309.

Sato, N., D. M. Wright, C. W. Carlson, Y. Ebihara, M. Sato, T. Saemundsson, S. Milan, *and* M. Lester *(*2004*),* Generation region of pulsating aurora obtained simultaneously by the FAST satellite and a Syowa-Iceland conjugate pair of observatories, J. Geophys. Res., 109, *A10201*, *doi:*10.1029/2004JA010419.

Schlegel, K., and J. P. St.-Maurice (1981), Anomalous heating of the polar E region by unstable plasma waves 1. Observations, J. Geophys. Res., 86(A3), 1447–1452, doi:10.1029/JA086iA03p01447.

Schunk, R. W., and A. Nagy (1978), Electron temperatures in the F region of the ionosphere: theory and observations, Rev. Geophys. 16, 355–399.

Scourfield, M. W. J.,J. G. Keys, E. Nielsen, C. K. Goertz, H. Collin (1983), Evidence for the E×B drift of pulsating auroras, J. Geophys. Res., 88, 7983-7988.

Semeter, J., M. Mendillo, and J. Baumgardner (1999), Multispectral tomographic imaging of the midlatitude aurora, J. Geophys. Res., 104(A11), 24565–24585, doi:10.1029/1999JA900305.

Solomon, S. C., P. B. Hays, and J. R. Abreu (1988), The auroral 6300 Å emission: Observations and modeling, J. Geophys. Res., 93(A9), 9867–9882, doi:10.1029/JA093iA09p09867.

Strangeway, R. J., R. E. Ergun, Y.-J. Su, C. W. Carlson, and R. C. Elphic (2005), Factors controlling ionospheric outflows as observed at intermediate altitudes, J. Geophys. Res., 110, A03221, doi:10.1029/2004JA010829.

Wu, S., R. E. Denton, and W. Li (2013), Effects of cold electron density on the whistler anisotropy instability, J. Geophys. Res., 118, 765–773, doi: 10.1029/ 2012JA018402.

Yando, K., R. M. Millan, J. C. Green, and D. S. Evans (2011), A Monte Carlo simulation of the NOAA POES Medium Energy Proton and Electron Detector instrument, J. Geophys. Res., 116, A10231, doi:10.1029/2011JA016671.

Yang, B., E. Donovan, J. Liang, and E. Spanswick (2017), Statistical study of the motion of pulsating aurora patches: using the THEMIS All-Sky Imager, Ann. Geophys., 35, 217-225, doi:10.5194/angeo-35-217-2017.

Yang, B., E. Donovan, J. Liang, J. M. Ruohoniemi, and E. Spanswick (2015), Using patchy pulsating aurora to remote sense magnetospheric convection, Geophys. Res. Lett., 42, 5083–5089, doi:10.1002/2015GL064700.

Yau, A. W., B. A. Whalen, and D. J. McEwen (1981), Rocket-borne measurements of particle pulsation in pulsating aurora, J. Geophys. Res., 86(A7), 5673–5681.

Zhang, B.-C., Kamide, Y., and R. Y. Liu (2003). Response of electron temperature to field-aligned current. J. Geophys. Res. 108, 1169.

Zhu, J., A. J. Ridley, and Y. Deng (2016), Simulating electron and ion temperature in a global ionosphere thermosphere model: Validation and modeling an idealized substorm, J. Atmos. Sol. Terr. Phys., 138, 243-260.

Zou, S. , A. Ridley, X. Jia, E. Boyd, M. Nicolls, A. Coster, E. Thomas, J. M. Ruohoniemi (2017), Multi-instrument observations of intense ion upflow fluxes associated with SED observed during the June 1, 2013 geomagnetic storm, *J. Geophys. Res.*, 122, doi:10.1002/ 2016JA023697.

Figure Captions

Figure 1. (a) Elevation angles and azimuths of the PFISR beams in Freg732_v01 experiment mode and in WorldDay35 experiment mode. The circle center denotes the radar location, and the numbered circles indicate the elevation angles. (b) AACGM projection of the beams.

Figure 2. The top panel shows the THEMIS ASI keogram along PFISR meridian. A horizontal dotted line shows the MLAT of Poker Flat. Three pronounced intervals of pulsating auroras that are active over PFISR are circled. The 2nd to bottom panels show the PFMSP observations of 630nm, 557.7nm, and 427.8 nm auroral intensity. The left-side y-labels of PFMSP panel give the elevation angle, while the MLATs are marked on the right-side, based on the assumption of emission height of 110 km for green/blue-line and 230 km for red-line aurora.

Figure 3. PFIFR observations on the field-aligned beam. The top panel shows the THEMIS ASI counts sampled around the beam footprint. The 2nd panel shows the PFMSP 557.7 nm (green), 427.8nm (blue), and 630nm (red) auroral intensities in the elevation bin along the beam. The bottom two panel show the T_e & N_e observations in long-pulse mode. We have marked the identified red-line intensification with arrow, and the pulsating auroral (PA) interval with vertical dotted lines.

Figure 4. The center sub-figure shows a THEMIS ASI image demonstrating the typical geometry of the patches with respect to PFISR beams. The other four sub-figures correspond to four selected beams (1,4,7,9) in the WorldDay35 mode: the top panel shows the THEMIS ASI ewogram constructed in the MLAT range of 300-500 km altitude bins of the beam; Red horizontal dotted lines mark the MLON range corresponding to 300-500 km altitude range of the beam. The bottom panels shows T_e observation on that beam. The passage interval of pulsating auroras over each beam is marked by vertical dotted lines. The arrangement of sub-figures is similar to the realistic geometry of those beams in MLAT/MLON: the left/right/ upper/bottom of the plot indicates the west/east/north/south directions, respectively.

Figure 5. (a) The top panel shows PFMSP 630 nm observations. The red-line structure of interest is marked with dashed ellipse. The bottom panel shows the THEMIS ASI counts sampled around the footprint of the 300-500 km altitude bins of the vertical beam. (b) PFISR T_e observations in four meridional beams; beam number is labeled in the left title. Beam-7 is the vertical beam, and beam-10 is most northward-pointing beam. A red dashed arrow marks the propagation of the density structure of interest. The pulsating auroral passage interval on each beam is labeled with two black dashed lines.

Figure 6. (a) Scatter plot of all PFISR T_e data sampled on vertical and field-aligned beams during 1145-1345 UT. The median value (diamond) is marked at each altitude bin. A horizontal bar indicates the extension from lower to upper quartiles. Different colors refer to four auroral categories, as labeled in the right of the plot. (b)-(e) T_e histogram sampled at 420-500 km for four auroral categories. A vertical solid

line marks the median value, while two dashed lines mark the lower and upper quartiles, of T_e distribution in each sub-figure. The mean and standard deviation of 630nm auroral intensity in each category is labelled in the title.

Figure 7. Scatter plot of PFIST T_e versus altitude sampled during (a) quiet-auroral intervals; (b) pulsating auroral intervals, and (c) red-line auroral intensification intervals. Color scale denotes the ratio between T_{e_err} and T_e. In each subfigure, the median value of T_e (diamond) is marked at each altitude bin. A horizontal bar indicates the extension from lower to upper quartiles; it is plotted slightly off the center altitude in (b) and (c) to avoid overlapping. The median T_e profile as well as the lower-upper quartiles during quiet-intervals are reproduced in blue curve & bar in (b) and (c) for comparison purpose.

Figure 8. Scatter plot of PFISR T_e averaged at altitudes > 200 km and PFMSP red-line intensity averaged over the PFISR time bin for (a) pulsating auroral intervals, and (b) red-line intensification intervals. Note the different range of x-axis (630 nm intensity).

Figure 9. Scatter plot of PFISR Ne versus altitude sampled during (a) quiet-auroral intervals; (b) pulsating auroral intervals, and (c) red-line auroral intensification intervals. The format and symbols are the same as in Figure 7.

Figure 10. Scatter plot of PFISR VLOS versus altitude sampled during (a) quiet-auroral intervals; (b) pulsating auroral intervals, and (c) red-line auroral intensification intervals. The format and symbols are the same as in Figure 6. Color scale indicates the fitting error of VLOS.

Figure 11. Top panel shows the THEMIS ASI counts sampled around the footprint of the 300-500 km altitude bins of the vertical beam; the 2nd and bottom panels show the PFISR T_e observation on the vertical beam in long-pulse mode (F-region) and AC-mode (E-region), respectively.

Figure 12. (a) A few selected THEMIS ASI images showing the passage of NOAA-19 satellite over the pulsating aurora of interest. (b) The top panel shows the along-track keogram of THEMIS ASI images; the satellite trajectory is marked as a red dotted line. The 2nd panel shows the direction flux in MEPED E1 channel. The 3rd panel shows the total electron precipitation energy flux in 1-20 keV (black) and 50-1k eV (red) energy ranges measured by TED. The 4th panel shows the max-flux energy bin of TED. The bottom panel shows the proton precipitation energy flux in 50-1000 eV energy range.

Figure 13. Simulation results of T_e profiles. Blue curve indicates the T_e profile corresponding to the ambient diffuse aurora, while the black curves represent the T_e profiles with inclusion of the pulsating auroral component, with two different heat fluxes set at the topside boundary of the ionosphere (labeled on each curve in the unit of eV/cm^2/s). For model details, see LJ17.

Table 1. Identified intervals for four types of auroral activities

		T_e & VLOS	N_e
Pulsating aurora	FA Beam	1219-1233	
		1248-1300	
		1303-1326	
	Vert. Beam	1217-1231	
		1251-1257	
		1311-1324	
Red-line intensification	FA Beam	1149-1151	1149-1153
		1201-1210	
		1213-1217	1213-1219
		1243-1247	1243-1249
		1326-1330	1326-1331
	Vert Beam	1149-1151	1149-1153
		1200-1209	
		1324-1328	1224-1330
Quiet aurora	FA Beam	1153-1200	
		1236-1243	
		1333-1345	N/A
	Vert Beam	1235-1245	
		1329-1345	N/A
Other	FA Beam	1145-1345 excluding the above three category intervals	
	Vert Beam	1145-1345 excluding the above three category intervals	

* All intervals are presented in format of HHMM in UT time.

* Sampling interval for N_e during short-lived red-line intensifications may be ~2 min longer than that for T_e & VLOS, for the rationale explained in the text.

Table 2. Respective roles of energetic and low-energy electrons from the magnetosphere in pulsating auroras and in the ionosphere

	Energetic electrons	**Low-energy electrons**
Role in patchy Pulsating aurora	(Along with produced secondaries) Auroral emission excitation and its on-off variation	Affecting chorus wave growth & propagation in flux tubes; Controlling the dimension & motion of the patch
Topside ionosphere	No effect	(Via collisions with and heat transfer to ionospheric electrons) Strong T_e enhancement and downward heat flux
F-region ionosphere	Small secondary electron flux; Small effects in T_e and N_e enhancement via secondary electron heating & ionization in upper F-region; Increasing effects towards lower altitudes	No penetrated secondaries; T_e enhancement in upper F-region via heat conduction from topside ionosphere; Decreasing effects towards lower altitudes
E-region ionosphere	T_e and N_e enhancement via secondary electron heating & impact ionization	No effect

(a)

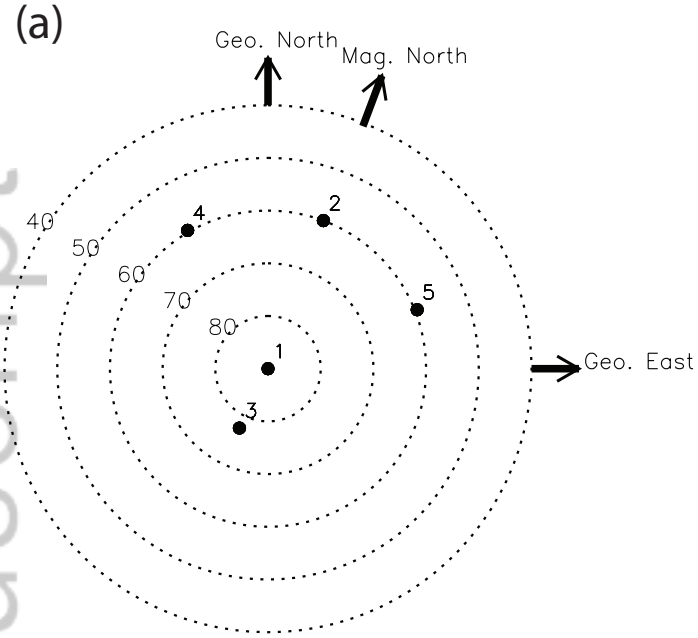

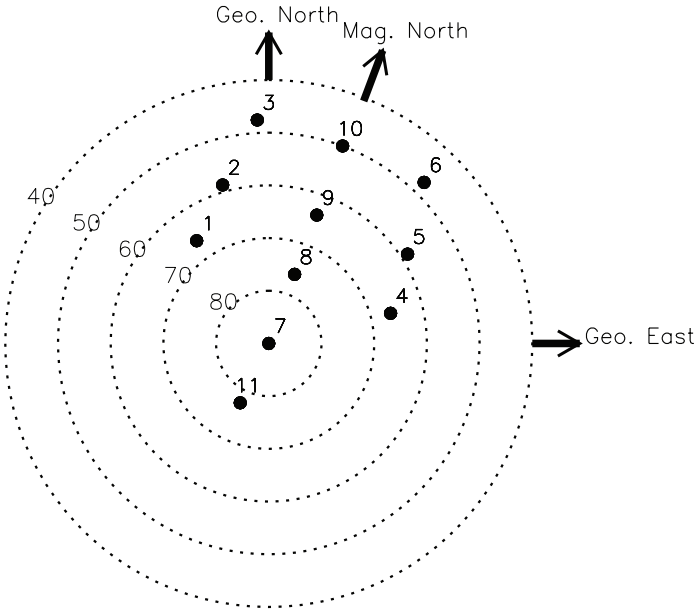

Freg732_v01 Experiment

WorldDay35 Experiment

(b)

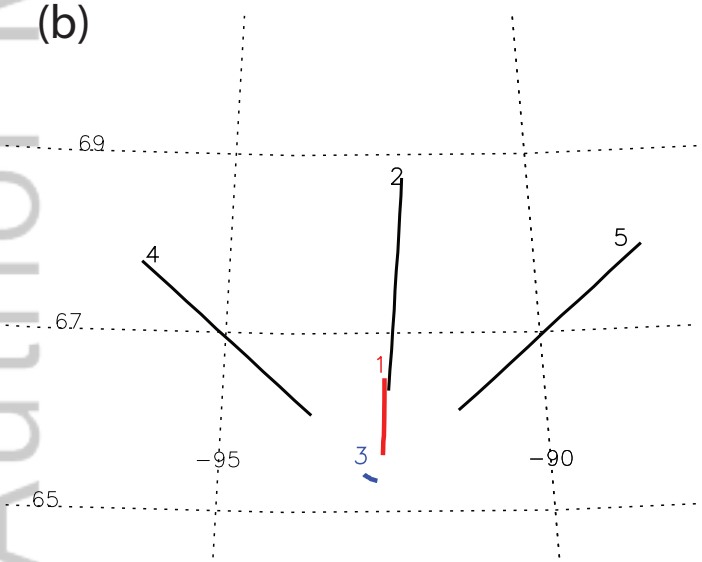

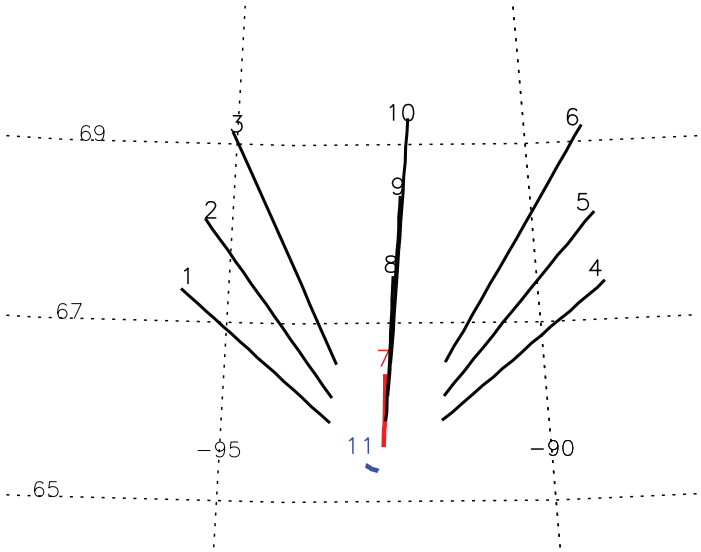

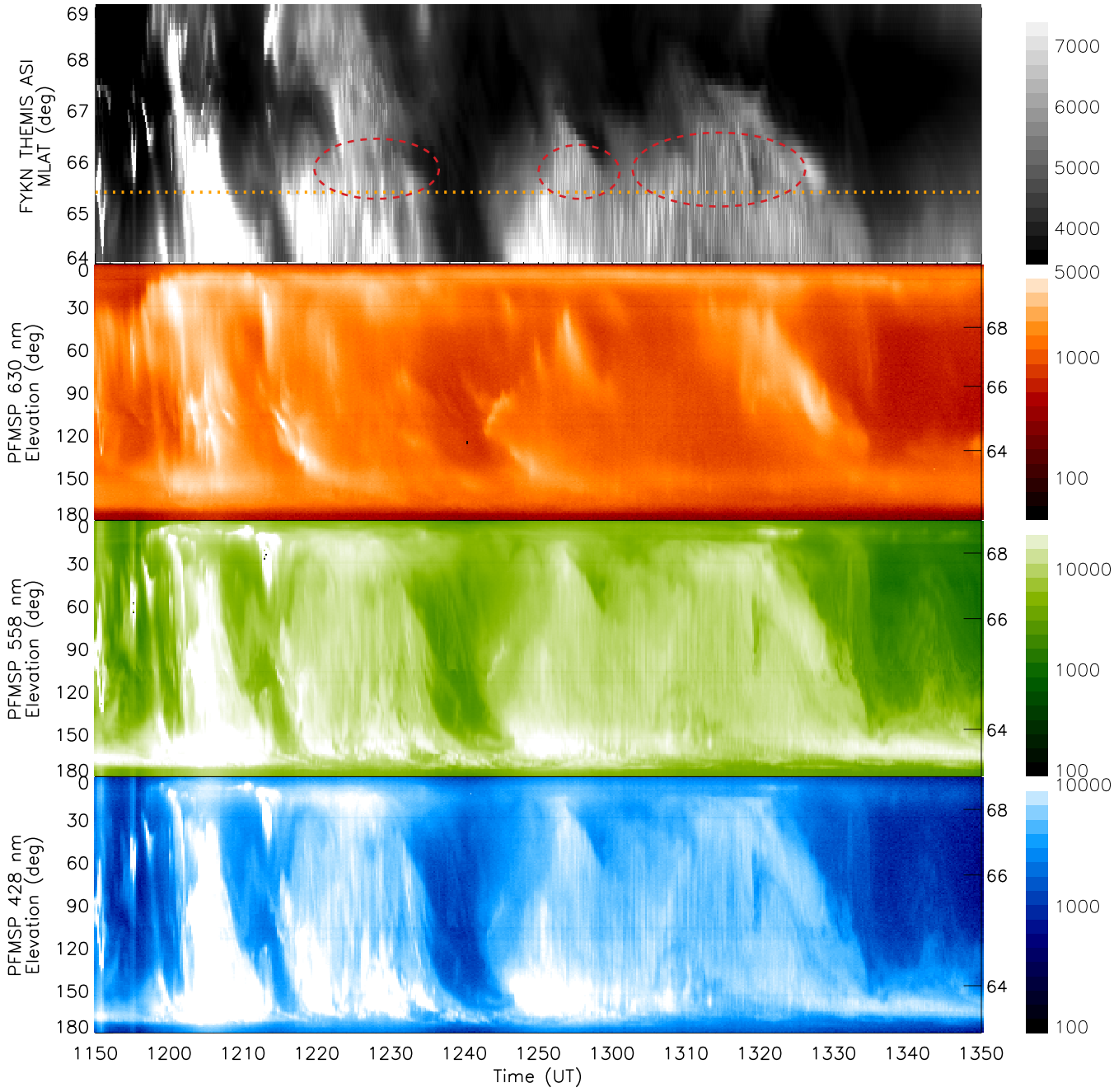

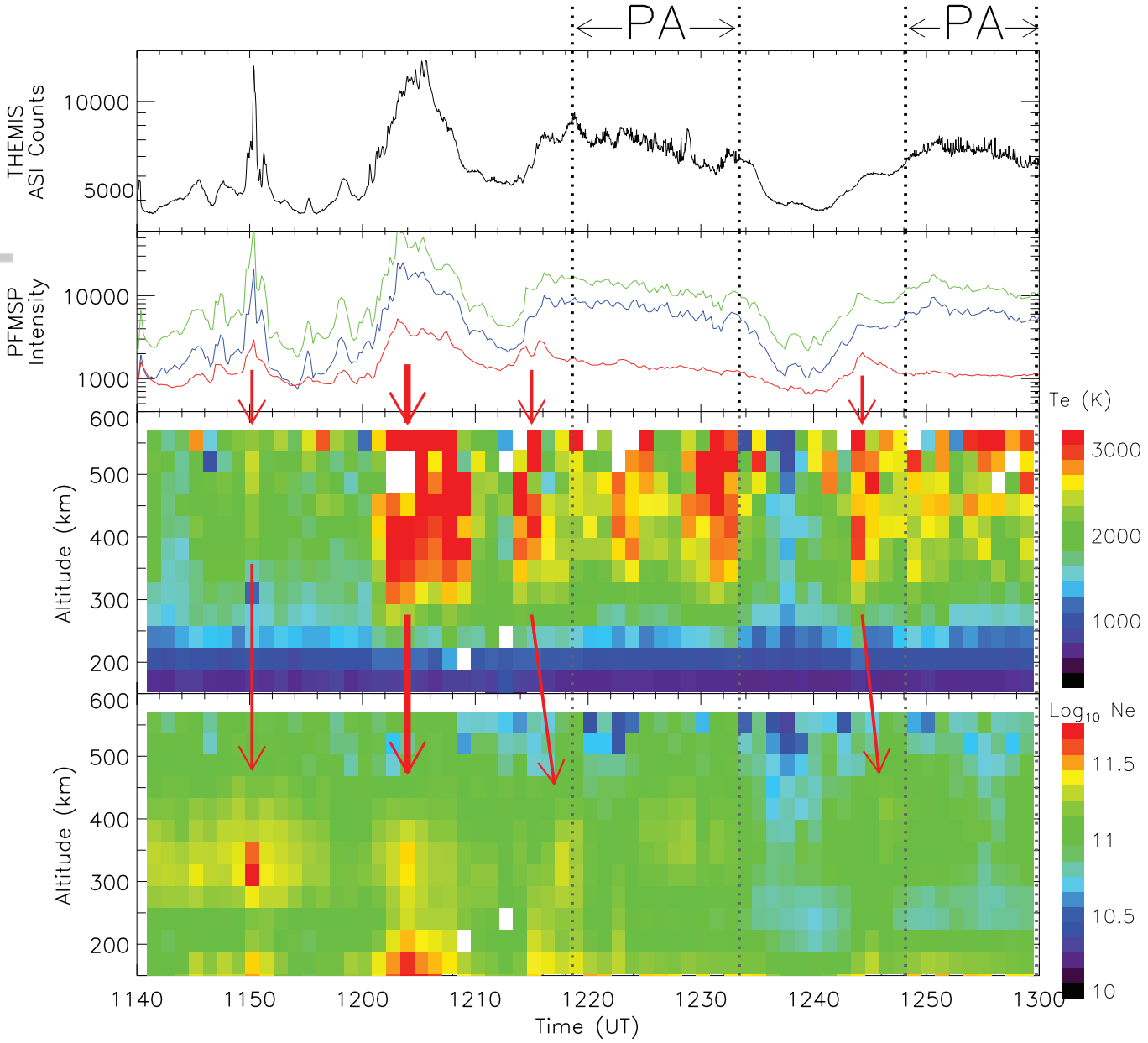

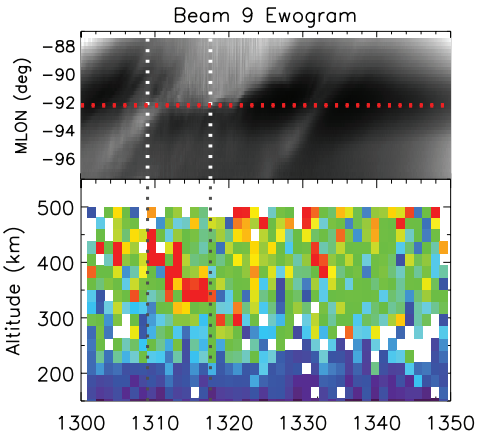

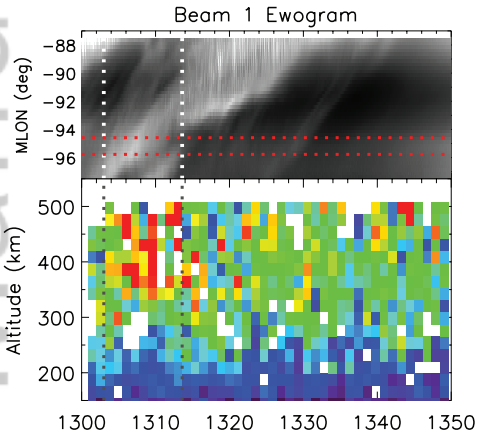

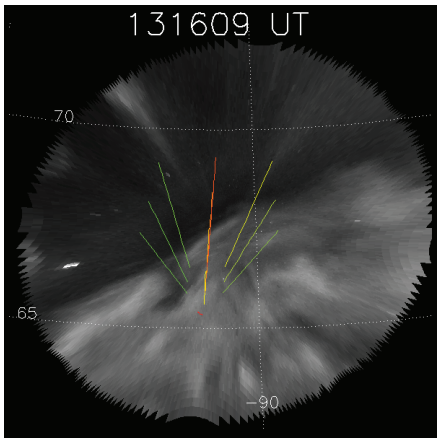

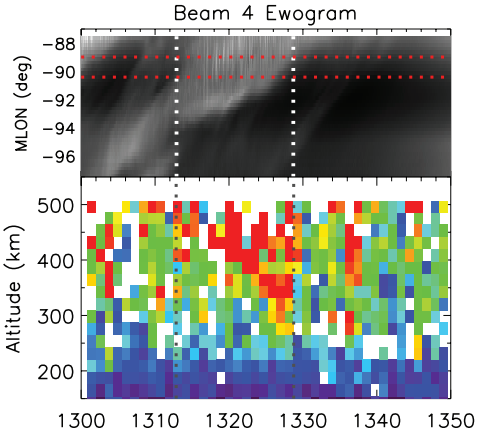

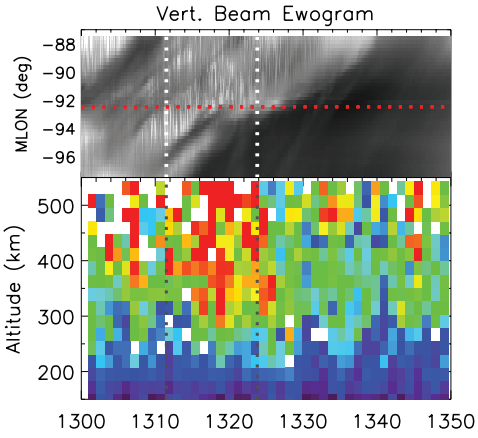

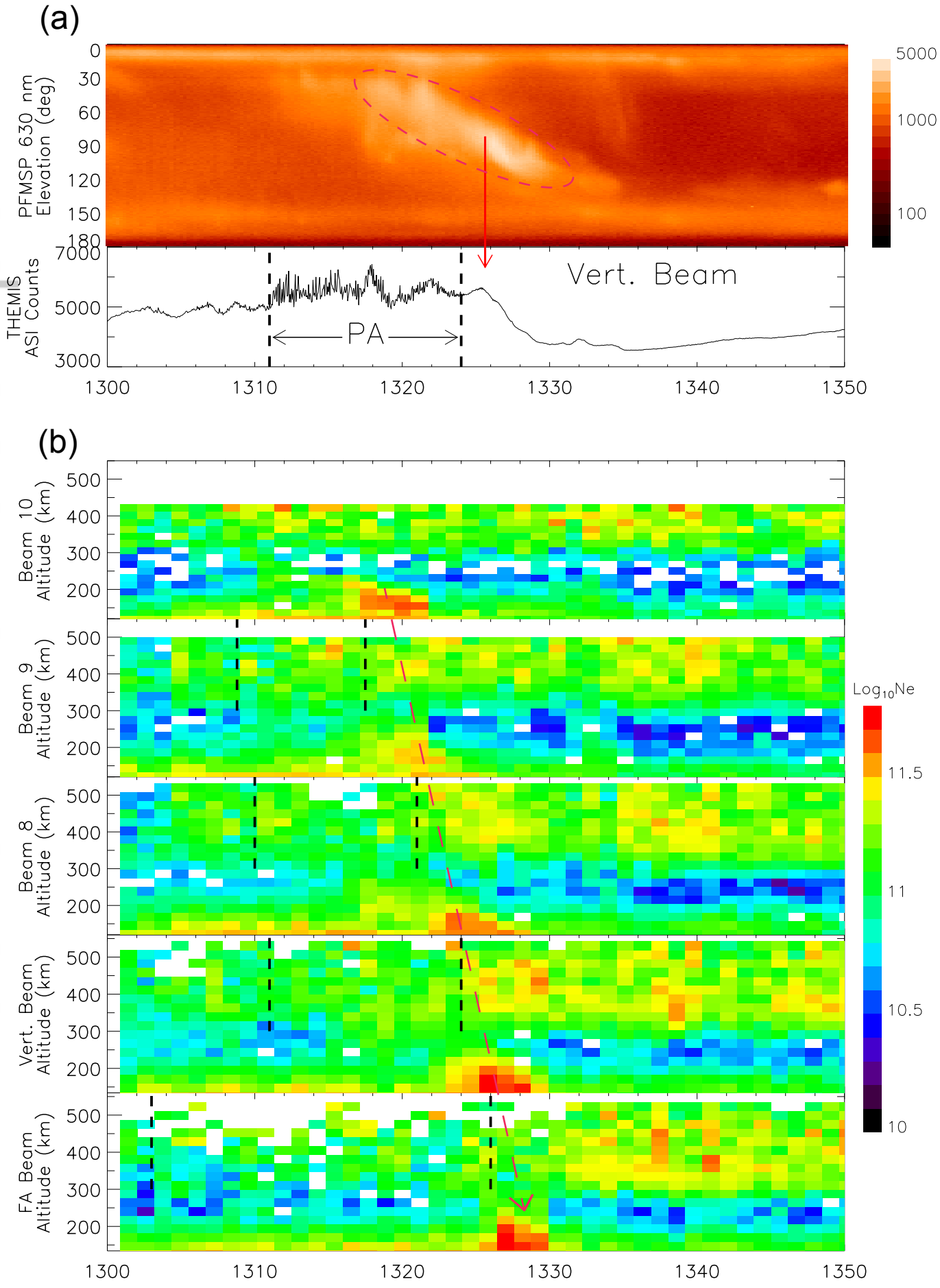

Figure 6

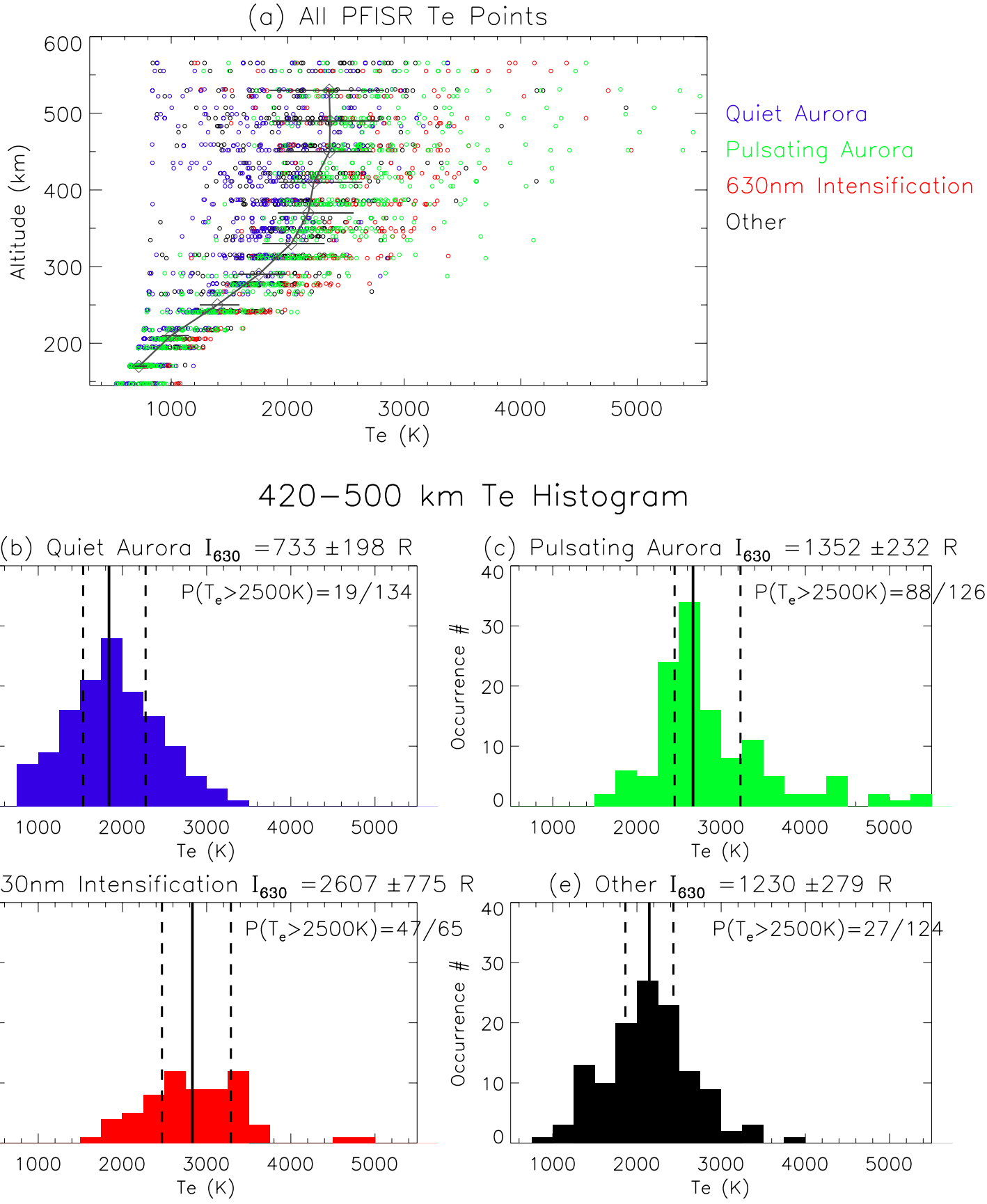

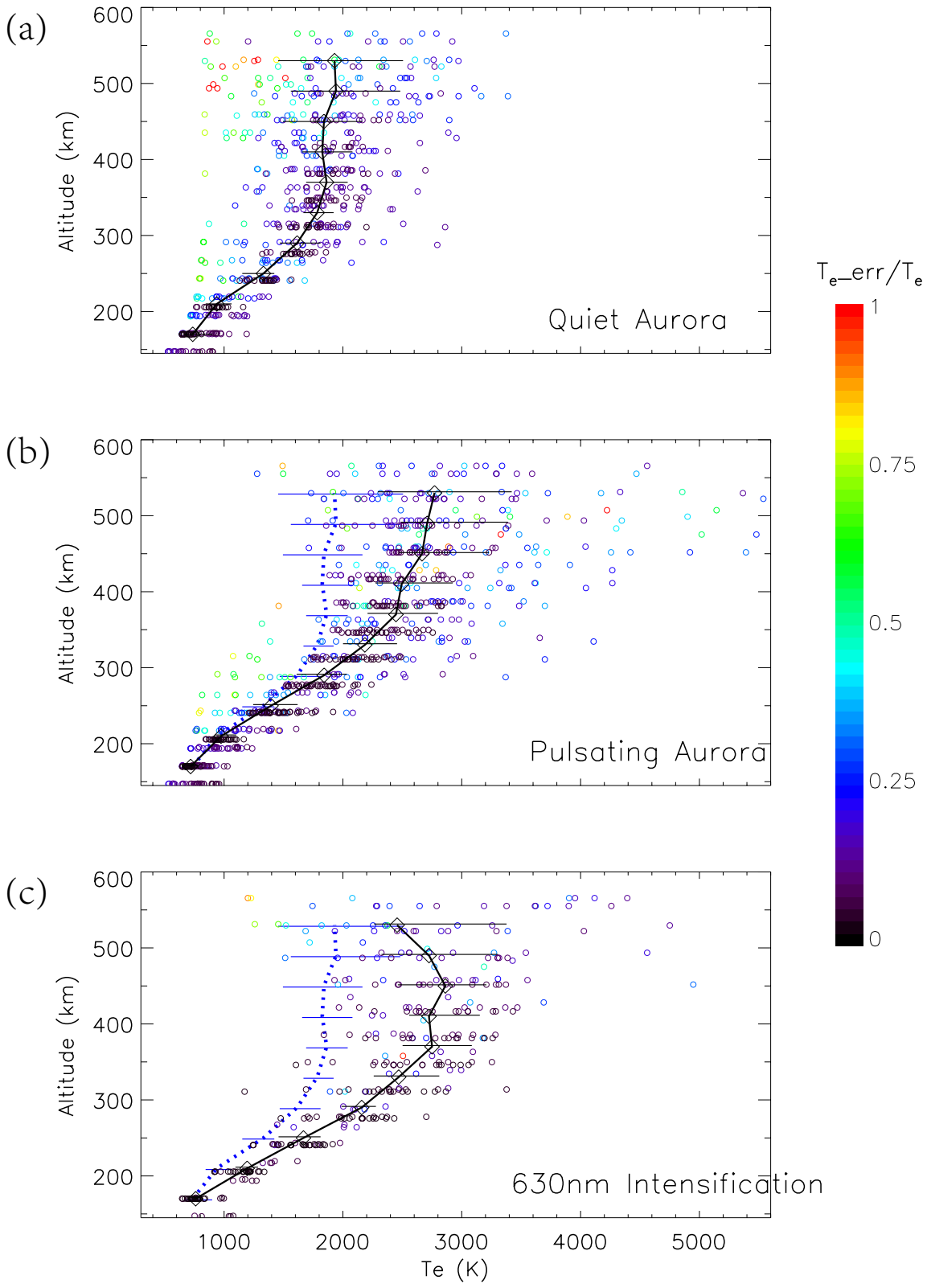

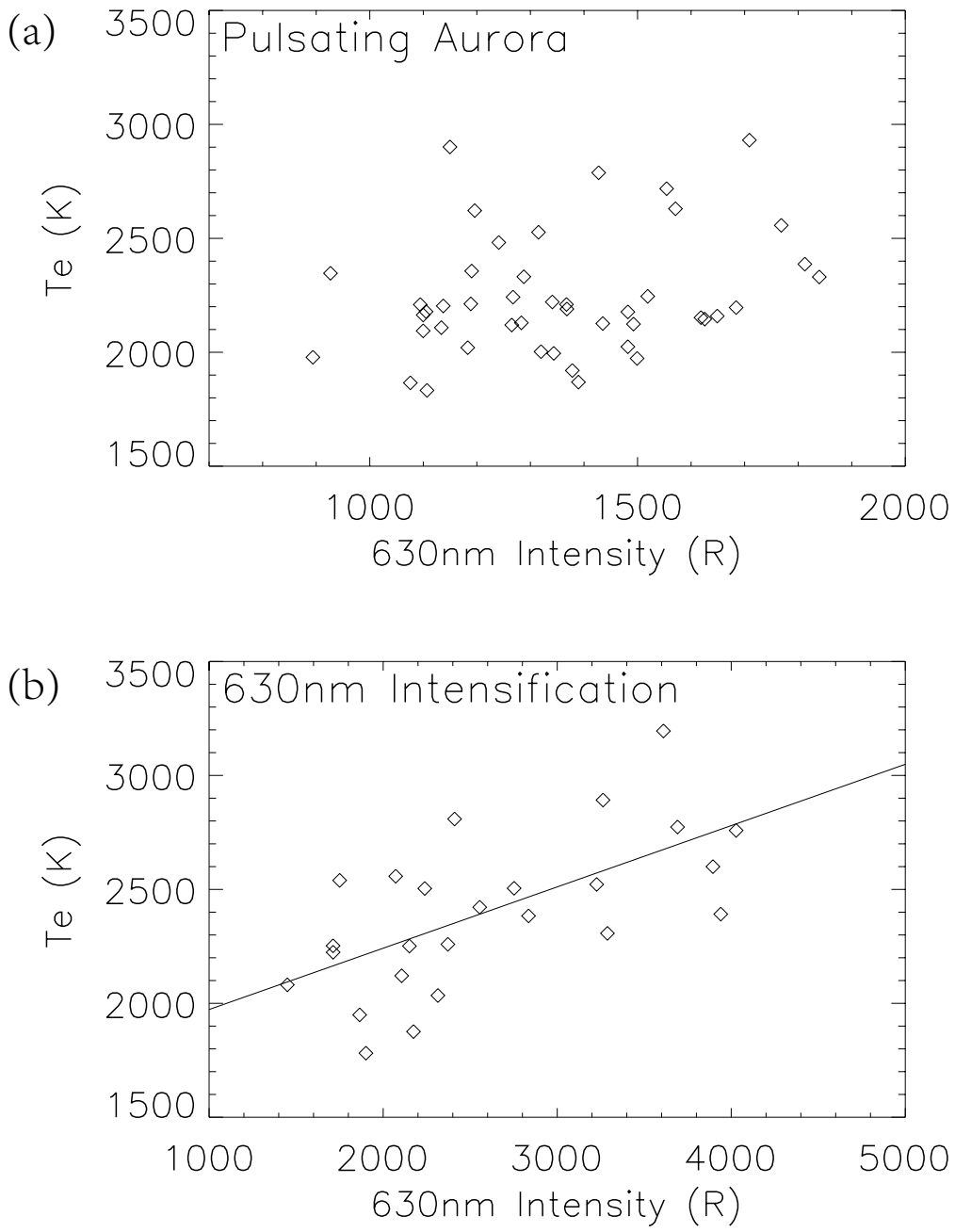

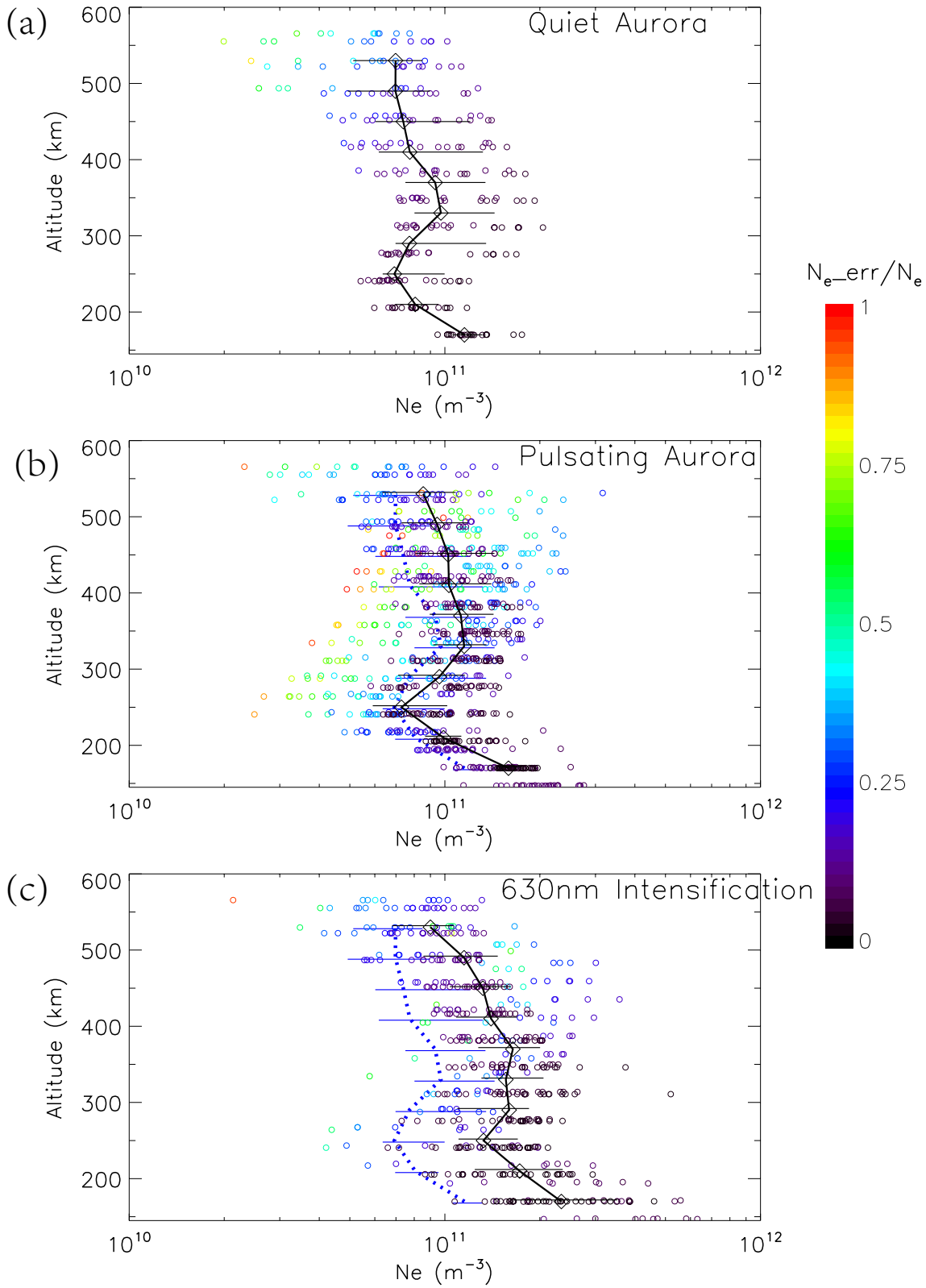

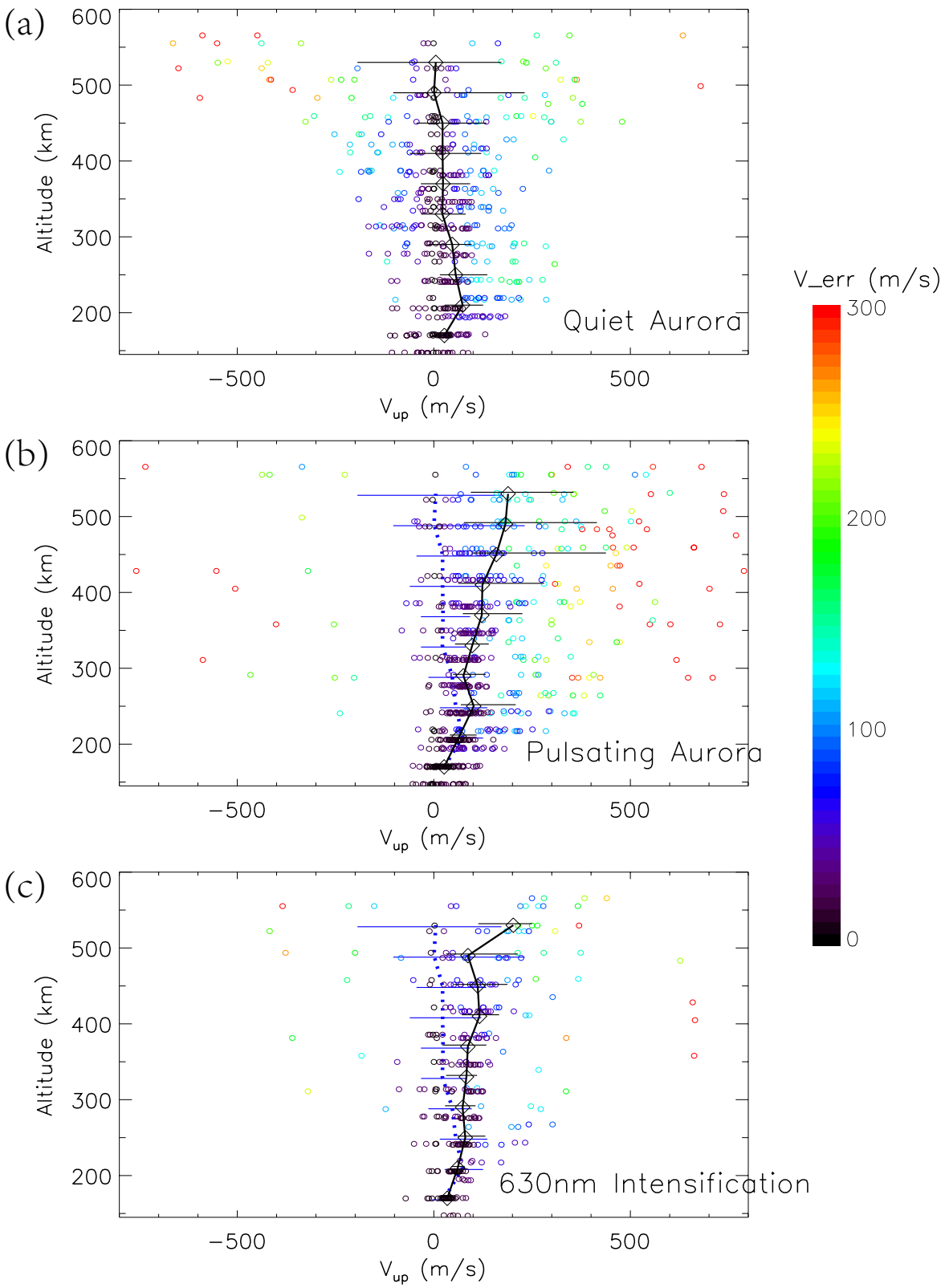

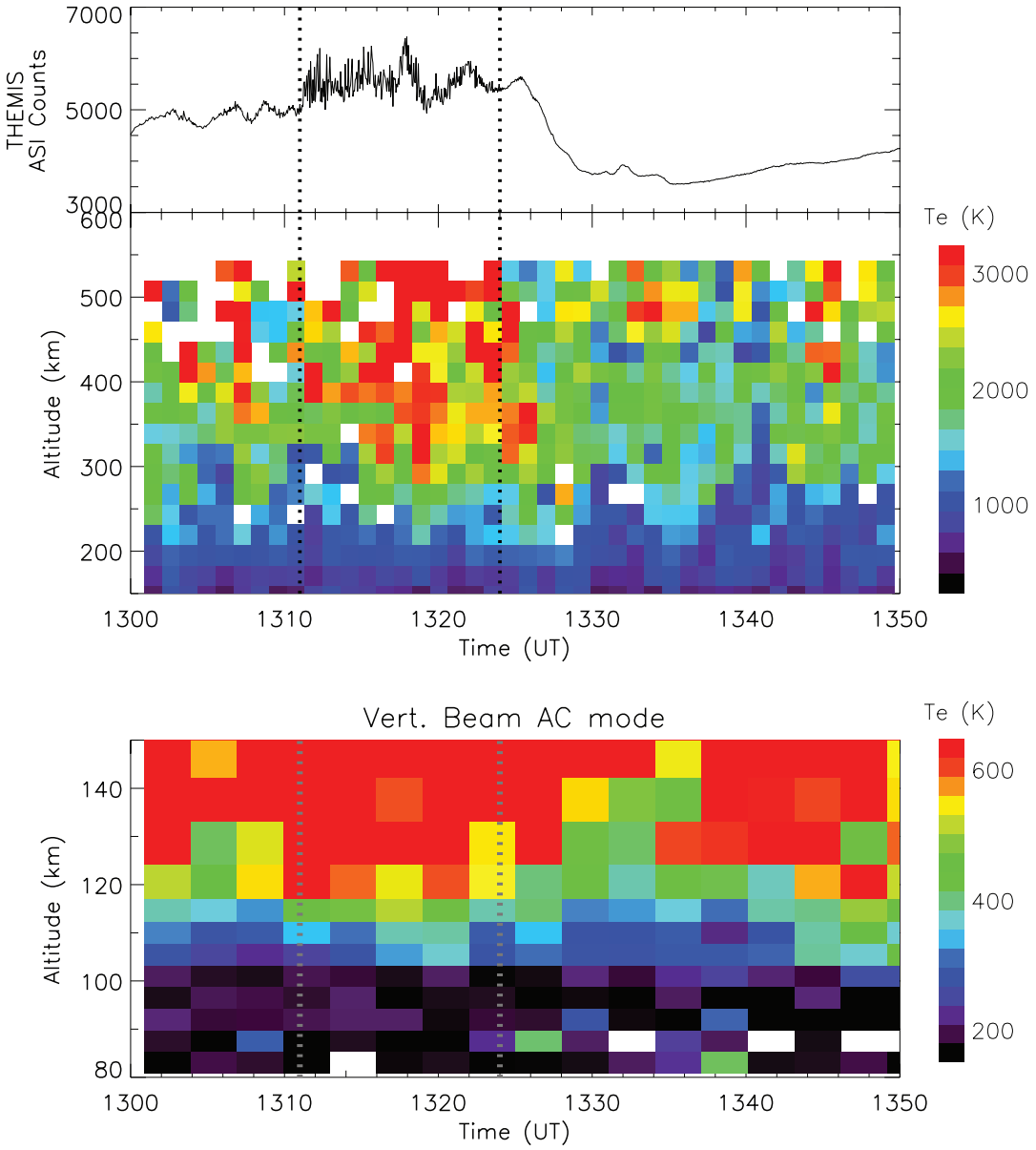

(a)

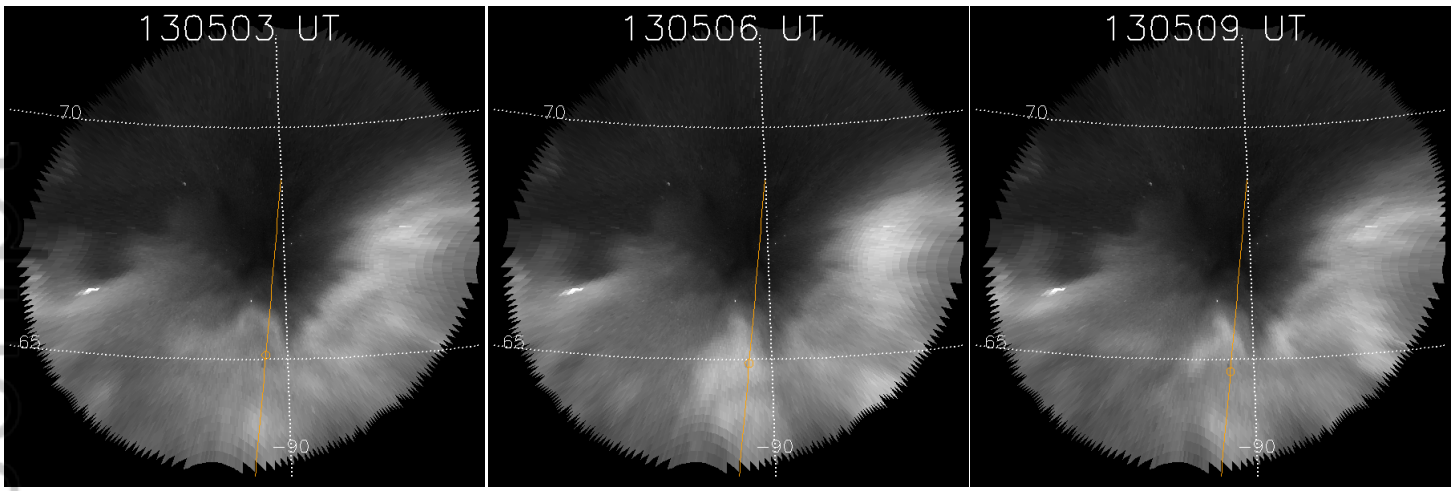

(b)